

# CCAV-10m: An Annual Spatiotemporal Dataset for Eastern Coastal China's Wetland Vegetation by Integrating Sentinel-1/2 Observations via deep learning

Yuying Li<sup>1,2</sup>, Lina Yuan<sup>1,2</sup>, Ting Liu<sup>1,2</sup>, Zijiang Song<sup>1,2</sup>, Shuang Yang<sup>1,2</sup>, Zilong Zhu<sup>1,2</sup>, and Min Liu<sup>1,2</sup>

<sup>1</sup>Key Laboratory of Geographic Information Science (Ministry of Education), East China Normal University, Shanghai 200241, China

<sup>2</sup>Key Laboratory of Spatial-temporal Big Data Analysis and Application of Natural Resources in Megacities (Ministry of Natural Resources), East China Normal University, Shanghai 200241, China

**Correspondence:** Lina Yuan (llyuan@geoai.ecnu.edu.cn) and Min Liu (mliu@geo.ecnu.edu.cn)

**Abstract.** Coastal wetland vegetation plays a vital role in shoreline protection and ecosystem management, highlighting the need for accurate and high-resolution mapping of these unique and vulnerable habitats. Here, we present CCAV-10m, the first publicly available annual species-level wetland dataset for eastern coastal China at 10 m resolution (2016–2023). This dataset was generated using a novel phenology-guided coastal wetland vegetation classification network (P\_SVCN), which integrates Sentinel-1/2 satellite imagery with extensive in situ observations. Validation based on 4,668 in situ samples confirms that P\_SVCN delivers strong classification performance, achieving an overall accuracy of 0.916 and a Kappa coefficient of 0.898. Spatiotemporal analysis of CCAV-10m reveals that *Suaeda* spp. is the dominant vegetation type, followed by *Spartina alterniflora*, whose coverage nearly equals the combined extent of *Phragmites australis*, mangroves, *Scirpus mariqueter*, and *Tamarix chinensis*. Notably, this work fills critical gaps in both spatial detail and temporal consistency across existing coastal wetland datasets, demonstrating the effectiveness of deep-learning-based fusion of optical and SAR data for high-resolution vegetation mapping. Regular updates to CCAV-10m will support long-term coastal wetland research, enhance invasive species monitoring, and inform wetland restoration and precision management efforts. The CCAV-10m dataset is openly accessible at <https://doi.org/10.57760/sciencedb.31077> (Li et al., 2025).

## 1 Introduction

Coastal wetlands are complex ecosystems distributed along the land–sea transition zone, influenced jointly by tidal dynamics and salinity gradients, and mainly comprise salt marshes, mangroves, tidal flats, and brackish wetland forests (Day et al., 2024; Bernhardt, 2022; Moreno-Mateos et al., 2012). Tropical mangroves cover approximately 150,000 km<sup>2</sup>, while temperate tidal marshes exceed 45,000 km<sup>2</sup> (Webb et al., 2013; Luther and Greenberg, 2009), together forming one of the most productive and carbon-rich ecosystems on earth (Macreadie et al., 2019; Bertram et al., 2021). Coastal wetlands function not only as geochemical “sinks” but also as highly effective “green filters” that intercept and remove land-derived pollutants (Sun et al., 2015; Zhang et al., 2022c). Their ecosystem service value can reach up to US\$194,000 per hectare per year, encompassing

carbon sequestration and greenhouse gas regulation, coastal protection, fisheries support, water purification, and biodiversity maintenance (Gabler et al., 2017; Schuerch et al., 2018; Costanza et al., 2014; Duarte et al., 2013; Aburto-Oropeza et al., 2008).

China's coastal wetlands represent a key component of its national blue carbon ecosystems, spanning tropical, subtropical, and temperate climate zones (Cao and Wong, 2007; Sun et al., 2015; Wang et al., 2021). Their broad distribution and substantial carbon sequestration capacity place them at the core of China's blue carbon strategy (Gu et al., 2025). Dominant vegetation types in Chinese coastal wetlands include *S. alterniflora*, *P. australis*, *T. chinensis*, *Suaeda spp.*, *S. mariqueter*, and mangroves (Gu et al., 2021). Among these, *S. alterniflora*, introduced in the 1990s, has rapidly expanded across Jiangsu, Shanghai, Zhejiang, and Fujian, with scattered occurrences in Liaoning, Tianjin, Hebei, and Shandong (Min et al., 2025; Chen et al., 2025). In many East Asian countries, biological invasions, tidal flat reclamation, and wetland restoration occur simultaneously; thus, timely and fine-scale species-level monitoring is crucial for tracking invasion dynamics, evaluating restoration outcomes, and supporting biodiversity conservation and sustainable coastal management (Tian et al., 2020; Sun et al., 2023).

Coastal wetlands are composed of herbaceous plants, grasses, and low-stature shrubs that are adapted to regular or occasional tidal inundation (Kumar and Sinha, 2014). Due to the inherent complexity of vegetation, tidal dynamics, and anthropogenic disturbances, mapping of coastal wetlands remains challenging (Zhao et al., 2023). To date, a variety of remote sensing data sources have been widely applied to monitor coastal wetland vegetation. In multispectral optical imagery, medium- to low-resolution datasets such as MODIS and AVHRR offer high temporal resolution (Gallo et al., 2005; Zhang et al., 2023a), which makes them suitable for wetland information extraction; however, their spatial resolution is insufficient for vegetation species-level classification (Takeuchi et al., 2003; Zhang et al., 2019). High-resolution optical imagery also plays an important role in wetland vegetation classification, but it is limited by cloud cover and atmospheric effects (Kang et al., 2023; O'Connell et al., 2017). Moreover, traditional remote sensing methods based on vegetation indices and phenological features are still widely applied. For example, the enhanced phenology-based vegetation index algorithm proposed by Zeng et al. (2022) achieved an overall accuracy of 86.67% for coastal salt marshes along the Bohai Sea, while Sun et al. (2023) applied a time-series model and phenological parameters to classify Jiangsu coastal salt marshes with an average overall accuracy of 84.8% ( $\pm 5.5\%$ ). Although these approaches are effective for short-term monitoring, they often struggle to capture complex spatial structures and inter-annual dynamics fully.

With the advancement of remote sensing technology, research on wetland vegetation classification has gradually shifted from traditional optical image-based methods to multi-source data fusion techniques. Synthetic Aperture Radar (SAR), with its all-weather and all-time imaging capabilities, has become a key complement to optical imagery (Van Beijma et al., 2014; Veloso et al., 2017). In recent years, researchers have attempted to integrate SAR and optical imagery to improve the accuracy of salt marsh vegetation classification. For instance, Xu et al. (2025) integrated Sentinel-1 SAR and Sentinel-2 optical imagery to classify wetland vegetation in the Yellow River Delta, China, achieving an overall accuracy of 93.51% and a Kappa coefficient of 0.917. Similarly, Slagter et al. (2020) combined Sentinel-1 SAR and Sentinel-2 for multi-level wetland classification in the St. Lucia Wetlands, South Africa, with an overall accuracy of 90.7%. At the same time, with the development of deep learning, convolutional neural networks and attention mechanisms have been increasingly applied to wetland vegetation classification, significantly improving spatial detail representation and cross-temporal feature extraction. For example, Sun et al. (2025)

employed a hybrid 2D–3D CNN to achieve an annual average classification accuracy exceeding 97% for Jiangsu coastal wetlands, and Li et al. (2021a) used a U-Net model to classify wetlands in South Carolina, USA, achieving a maximum accuracy of 90%. Although these regional studies have achieved promising results, they mostly focus on single-date or short-term analyses. Therefore, long-term, species-level wetland monitoring at a national scale remains limited, which is crucial for coastal ecosystem management and wetland conservation.

In this study, we developed a novel phenology-guided coastal wetland vegetation classification network integrating Sentinel-1/2 (P\_SVCN) based on deep learning and employed it to generate the CCAV-10m dataset (<https://doi.org/10.57760/sciencedb.31077>, Li et al., 2025), an annual spatiotemporal China’s coastal wetland vegetation dataset, 2016–2023. The P\_SVCN model integrates Sentinel-1 and Sentinel-2 imagery with in situ data, maintaining the sensitivity of SAR data to vegetation structure and moisture while adaptively incorporating the spectral and phenological information from optical imagery. P\_SVCN significantly improves classification accuracy, enabling species-level mapping of coastal wetland vegetation. CCAV-10m provides a valuable spatiotemporal resource for long-term monitoring, ecological research, and sustainable management of China’s coastal wetlands.

## 70 2 Study area

The Chinese coastline extends approximately 32,000 km, including 14,000 km of island coastlines, ranging from the Yalu River estuary in northern Liaoning Province to the Beilun River estuary in southern Guangxi and Hainan Island (Gu et al., 2021, 2025). This study focuses on eight coastal provinces and municipalities: Liaoning, Hebei, Tianjin, Shandong, Jiangsu, Shanghai, Zhejiang, and Fujian, spanning 23°30′– 40°03′ N latitude and 115°50′– 124°22′ E longitude (Fig. 1). The study area covers both temperate and subtropical climatic zones, supporting a diverse range of wetland vegetation types (Hu et al., 2021). Wetland boundaries were delineated using the GLC\_FCS30D dataset (Zhang et al., 2023b), with a 10 km buffer inland and seaward from the coastline applied for analysis. Common wetland species include *S. alterniflora*, *P. australis*, *T. chinensis*, *Suaeda spp.*, *S. mariqueter*, and mangroves (Chen et al., 2022). *S. alterniflora*, native to the Americas, was introduced to China in the 1990s and is now widespread in Jiangsu, Shanghai, Zhejiang, and Fujian, with scattered occurrences in Liaoning, Tianjin, Hebei, and Shandong (Min et al., 2025; Chen et al., 2025). *S. mariqueter* occurs mainly in Shanghai, Jiangsu, and the Hangzhou Bay area (Sun et al., 2025; Zheng et al., 2023), while *T. chinensis* and *Suaeda spp.* are concentrated in northern provinces (Sun et al., 2021), and mangroves are restricted to the southern coast, reaching their northern limit in Yueqing, Zhejiang (Wei et al., 2024).

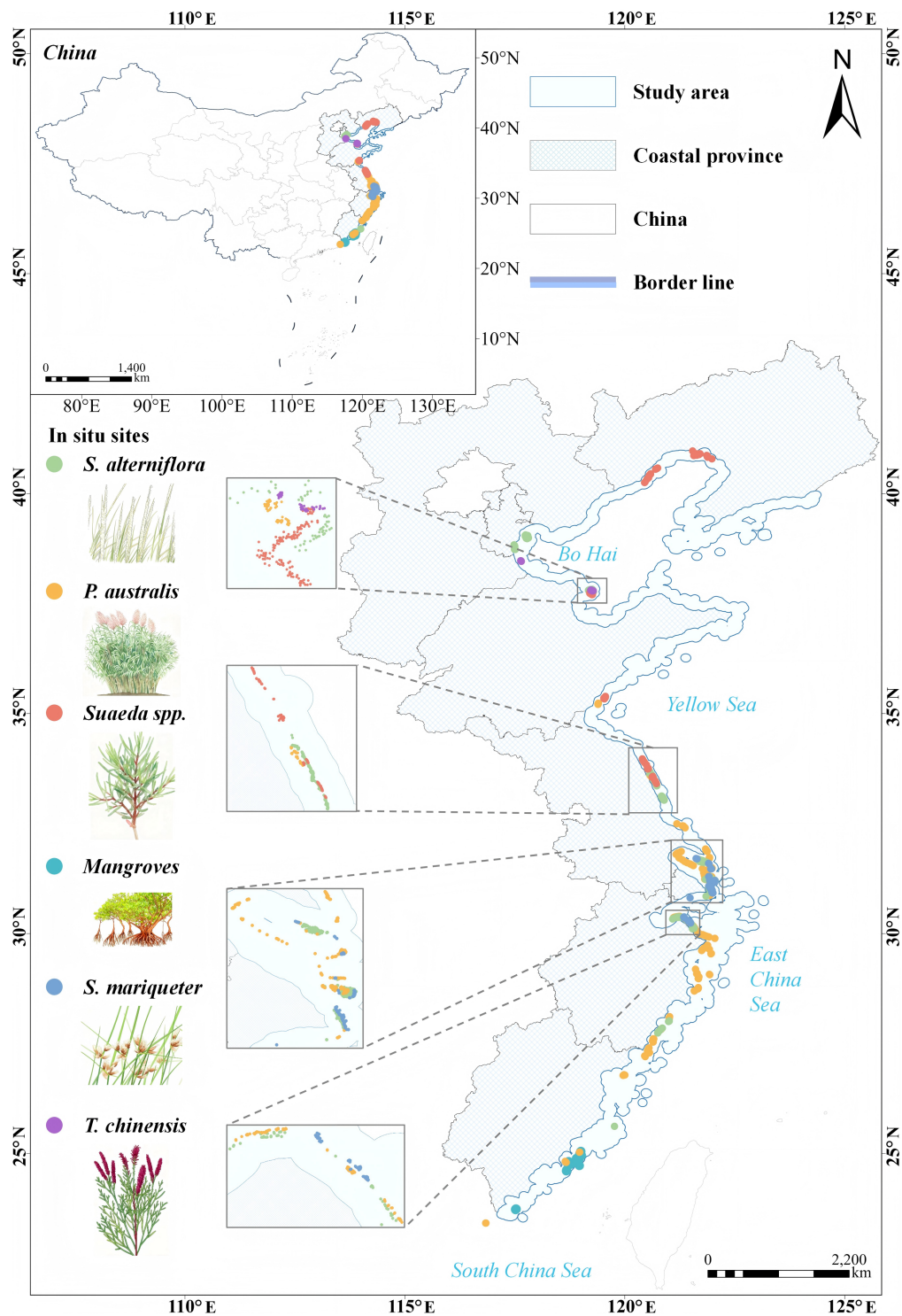


Figure 1. Location of the study area along the Chinese coastline, showing the extent of the coastal zone and the distribution of in situ wetland sampling sites.

### 3 Data and methods

#### 85 3.1 Sentinel-1

We used multisource remote sensing data, including Sentinel-1 and Sentinel-2 imagery, to improve coastal vegetation classification (Zhao et al., 2024). Sentinel-1 Level-1 Ground Range Detected (GRD) data (Potin et al., 2015) at 10 m resolution were preprocessed in SNAP following orbital correction, thermal noise removal, radiometric calibration, speckle filtering, and terrain correction, with reflectivity converted from linear scale to decibels (dB) (Li et al., 2024b). A total of 8,018 scenes spanning January 2016 to December 2023 in eastern China were composited annually using a mean function. These composites captured regional climatic patterns while reducing tidal and seasonal variability in salt marsh vegetation.

#### 3.2 Sentinel-2

Sentinel-2 imagery was selected according to the key phenological stages of coastal vegetation, namely green and senescence (Zhao et al., 2023). To ensure high spectral fidelity, a stringent cloud-cover threshold of less than 10% was applied during the scene selection process. Across the study period, 320 high-quality scenes of dual-temporal optical imagery were processed in SNAP and ENVI, including resampling and band fusion (Wang et al., 2024). Distinct from the year-round continuous observation strategy employed for Sentinel-1 SAR data, this targeted sampling of dual-phase optical imagery aims to capture the maximum inter-species spectral contrast while minimizing atmospheric interference.

For each phenophase, four spectral bands with the highest vegetation contrast—B02 (blue), B03 (green), B04 (red), and B08 (near-infrared)—were extracted, yielding eight optical channels (Bao et al., 2025). Normalized Difference Vegetation Index (NDVI) maps were derived from the red and near-infrared bands of both phenophases to capture differences in vegetation status. All SAR and optical images were co-registered and resampled to a consistent 10 m resolution to ensure data alignment and comparability.

#### 3.3 In situ data

105 We conducted field surveys and vegetation sampling across wetlands along the coast of eastern China, between 2017 and 2018. High-precision GPS (Trimble Juno 3D) and a DJI Phantom-4 RTK unmanned aerial vehicle were combined to systematically record site information. Following a stratified sampling design, plots were established for six representative salt marsh vegetation types: *P. australis*, *S. alterniflora*, *Suaeda spp.*, *T. chinensis*, mangroves, and *S. mariqueter*. Each plot measured 10 × 10 m, with a minimum distance of 100 m between adjacent plots to ensure spatial independence and representativeness. Within each plot, three 0.5 × 0.5 m quadrats were randomly located. GPS coordinates of each quadrat were recorded with ±5 m accuracy to guarantee even spatial coverage across vegetation types. Plot locations were further verified and corrected using high-resolution imagery from Google Earth to ensure consistency with actual vegetation distribution. To complement the field data, we also compiled additional wetland vegetation validation points from the literature (Zhao et al., 2023; Li et al., 2021b; Sun, 2023).

115 In total, 2,665 ground truth points were collected (Fig. 1), comprising 948 *S. alterniflora*, 678 *P. australis*, 432 *Suaeda spp.*,  
226 *S. mariqueter*, 263 mangrove, and 118 *T. chinensis* points. Experienced researchers then conducted visual interpretation and  
manual labeling of additional points using Google Earth imagery, resulting in 2,072 *S. alterniflora*, 2,435 *P. australis*, 2,632  
*Suaeda spp.*, 2,901 *S. mariqueter*, 1,803 mangrove, and 1,050 *T. chinensis* points. Collected samples underwent systematic  
quality control, producing a reliable dataset for training and validating remote sensing classification models.

### 120 **3.4 A phenology-guided coastal wetland vegetation classification network integrating Sentinel-1/2 (P\_SVCN)**

In this study, we developed a phenology-guided coastal wetland vegetation classification network integrating Sentinel-1/2  
(P\_SVCN) with a dual-branch multi-source attention mechanism for the fine-scale classification of coastal wetland vegeta-  
tion along the Chinese coast. The training dataset was based on Sentinel-1 imagery from 2017–2018, including VV and VH  
polarizations, along with three derived SAR features (SAR-Diff, SAR-NDVI, and SAR-SUM). Simultaneously, dual-phase  
125 Sentinel-2 optical imagery was incorporated, extracting eight spectral bands (B02, B03, B04, and B08 at two phenological  
phases) and their corresponding NDVI indices as input features. Vegetation types recorded at the sampled locations corre-  
sponding to the imagery periods were used as ground truth for supervised training. The dataset was strictly split into training  
(70%, 10,890 samples) and validation (30%, 4,668 samples) subsets. The trained model was then applied to classify coastal  
wetland vegetation from 2016 to 2023 along the Chinese coast.

#### 130 **3.4.1 SAR feature construction from Sentinel-1**

Sentinel-1 SAR imagery offers significant advantages for monitoring wetland vegetation, being highly sensitive to key vari-  
ables such as total vegetation water content, canopy structure dynamics, and vegetation cover (Vreugdenhil et al., 2018; Zhang  
et al., 2022a). With its all-weather, all-time radar observation capability, Sentinel-1 can reliably acquire data under diverse me-  
teorological conditions, providing robust support for temporal analyses of vegetation dynamics (Simioni et al., 2020; Mleczko  
135 and Mróz, 2018). The C-band radar signals can penetrate the canopy and effectively capture interactions between vegetation  
and soil (Mao et al., 2023), making Sentinel-1 particularly suitable for long-term monitoring and dynamic studies of wetland  
ecosystems (Yang and Guo, 2019; Zhang et al., 2021).

Backscatter coefficients in VV and VH polarization provide insight into vegetation–ground interactions (Vreugdenhil et al.,  
2018; Mandal et al., 2020; Nikaein et al., 2021). Vegetated areas typically exhibit higher surface roughness than non-vegetated  
140 regions, resulting in distinct backscatter differences, although VH polarization signals may be influenced by double-bounce  
effects from soil surfaces (Veloso et al., 2017; Ferro et al., 2011). To suppress the inherent speckle noise in SAR imagery and  
capture stable annual structural signatures of coastal vegetation, we utilized all available Sentinel-1 scenes acquired throughout  
the entire study year. An annual mean compositing strategy was applied to generate a representative backscatter coefficient for  
each pixel. Based on these considerations, this study utilized the processed VV and VH single-polarization SAR data along  
145 with three derived indices, including SAR\_NDVI, SAR\_SUM, and SAR\_Diff, for the classification of wetland vegetation types  
along eastern China’s coastal zones.

SAR\_NDVI quantifies normalized differences in backscatter coefficients between VV and VH polarization states, providing a reliable basis for distinguishing vegetation types (Veloso et al., 2017). SAR\_Diff effectively suppresses double-bounce effects from straw or surface structures, enhancing the ability to detect subtle differences between vegetation and soil, thereby improving classification accuracy (Mahdianpari et al., 2020). SAR\_SUM integrates the total backscatter intensity from both VV and VH channels, offering a comprehensive representation of canopy and surface structure information (Li et al., 2024b).

### 3.4.2 Phenology-based spectral feature extraction from Sentinel-2

The dominant vegetation types in different climatic zones exhibit distinct phenological rhythms (Zhang et al., 2022b). In temperate regions, vegetation growth is constrained by low temperatures and dormancy periods, resulting in a relatively concentrated growing season (Luo et al., 2025), whereas in subtropical regions, the growing period is prolonged and phenological transitions are relatively gradual. Using imagery acquired at a uniform time across the entire coastal zone would lead to phenological mismatches among regions, thereby increasing spectral confusion and classification errors (Zeng et al., 2022). Therefore, this study adopted a climate-zone-based strategy, selecting paired images corresponding to the green and senescence stages within each zone to enhance the spectral separability among vegetation types. To fully leverage the spectral differences of coastal wetland vegetation across phenological stages (Gao et al., 2023; Fu et al., 2025), dual-phase optical imagery was selected based on the growth patterns of representative vegetation within each climatic zone.

The annual NDVI time series for the dominant coastal vegetation species across eastern China's coastal zones. (Fig. 2) clearly reveal distinct seasonal dynamics for each species. The temperate zone was defined as the area north of the Qinling-Huaihe line (approximately 33°N), where the mean January temperature is below 0 °C (Almond et al., 2009; Chen et al., 2013), primarily including the coastal provinces of Liaoning, Tianjin, Hebei, Shandong, and northern Jiangsu. The North Subtropical zone extends from the Qinling-Huaihe line southward to the northernmost mangrove distribution in Yueqing, Zhejiang ( $\approx 28^{\circ}21'N$ ) (You et al., 2022), covering southern Jiangsu, Shanghai, and northern Zhejiang. The Subtropical zone lies south of this boundary, encompassing southern Zhejiang and Fujian provinces. For the temperate, North Subtropical, and Subtropical regions, two key time points ( $t_1$  and  $t_2$ ) corresponding to the peak growth and senescence stages were identified. Within each climatic zone, the dual-phase selection was kept consistent to ensure uniform input features. For spectral feature construction, four key optical bands—blue (B2), green (B3), red (B4), and near-infrared (B8)—were extracted for each pixel at both phenological stages, and the Normalized Difference Vegetation Index (NDVI) was calculated from the red and near-infrared bands (Eq. 1). The dual-phase optical bands and corresponding NDVI values were then combined into a spectral feature vector (Eq. 2).

$$NDVI = \frac{NIR - Red}{NIR + Red} \quad (1)$$

$$\mathbf{F}_{\text{spectral}} = [B2_{t1}, B3_{t1}, B4_{t1}, B8_{t1}, NDVI_{t1}, B2_{t2}, B3_{t2}, B4_{t2}, B8_{t2}, NDVI_{t2}] \quad (2)$$

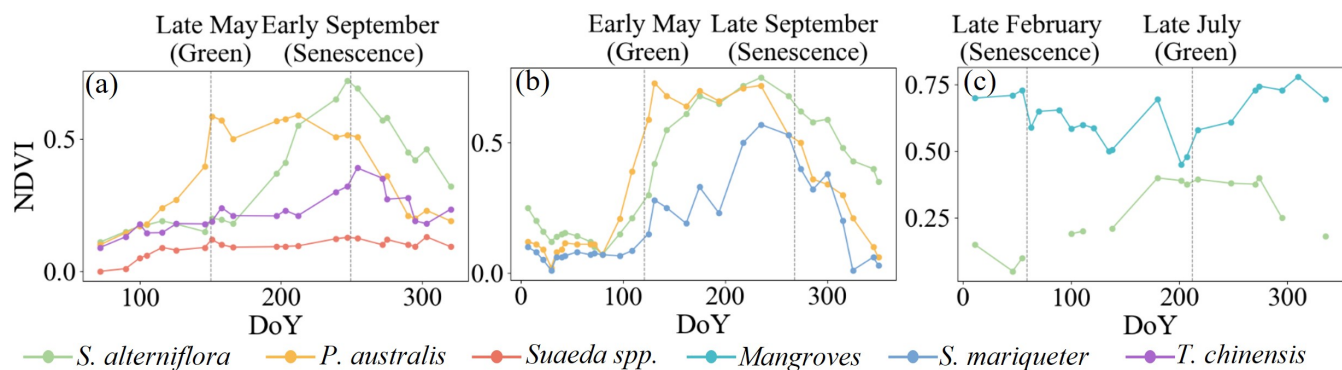


**Figure 2. Seasonal NDVI profiles of dominant coastal wetland vegetation in eastern China.** (a) Temperate, (b) North Subtropical, and (c) Subtropical zones. Each profile represents the mean NDVI calculated from all validated samples within the respective region. Distinct annual NDVI variations were observed among the main vegetation types (*S. alterniflora*, *P. australis*, *Suaeda spp.*, *S. mariqueter*, *T. chinensis*, and mangroves), which guided the dual-phase selection summarized in Tab 1. Note that temporal gaps in the *S. alterniflora* profile in (c) are due to the exclusion of low-quality pixels caused by frequent precipitation and tidal inundation in low-latitude regions, ensuring the purity of phenological signatures.

**Table 1. Dual-phase phenological signatures of wetland vegetation across different climatic zones in eastern China.** This table summarizes the representative vegetation species, the selected phenological phases, and the rationale for determining optimal dual-phase optical imagery across the temperate, north subtropical, and subtropical regions.

Climatic Zone	Vegetation Types	Phase 1 (Green)	Phase 2 (Senescence)	Selection Rationale
Temperate (Liaoning, Tianjin, Hebei, Shandong, Jiangsu)	<i>S. alterniflora</i> , <i>P. australis</i> , <i>Suaeda spp.</i> , <i>T. chinensis</i>	Late May	Early September	Late May: <i>P. australis</i> greening advanced while <i>S. alterniflora</i> has not peaked; Early September: <i>S. alterniflora</i> near peak and <i>P. australis</i> declining. Maximizes phenological contrast between <i>P. australis</i> and <i>S. alterniflora</i> , and distinguishes <i>T. chinensis</i> (low NDVI) from consistently low NDVI <i>Suaeda spp.</i>
North Subtropical (Jiangsu, Shanghai, north of Yueqing, Zhejiang)	<i>S. alterniflora</i> , <i>P. australis</i> , <i>S. mariqueter</i> , <i>Suaeda spp.</i>	Early May	Late September	Early May: growth differences among <i>S. mariqueter</i> , <i>P. australis</i> , and <i>S. alterniflora</i> are pronounced; Late September: senescence differentiates <i>P. australis</i> and <i>S. alterniflora</i>
Subtropical (Zhejiang, Fujian)	<i>S. alterniflora</i> , mangroves	Late July	Late February	Late July: <i>S. alterniflora</i> at peak, distinguishable from evergreen mangroves; Late February: <i>S. alterniflora</i> NDVI lowest, clearly distinguishable from mangroves.

### 3.4.3 Network framework of the P\_SVCN

Coastal wetland vegetation often exhibits high spectral similarity, further complicated by tidal fluctuations, salinity gradients, and seasonal phenology, which challenge accurate classification (Gao et al., 2023; Fu et al., 2025). To address this, we developed a phenology-guided coastal wetland vegetation classification network integrating Sentinel-1/ (P\_SVCN), which employs a dual-branch multi-source attention fusion design to enhance feature representation (Fig. 3). One branch processes Sentinel-1 SAR bands and their derived indices, while the other handles Sentinel-2 optical bands and phenological features. Features from both branches interact through the SAR–Optical Cross-Source (SOCS) Block. Let the output features of the SAR branch be  $F_{\text{SAR}}$  and those of the optical branch be  $F_{\text{Optical}}$ , projected into query ( $Q$ ), key ( $K$ ), and value ( $V$ ) spaces as in Eq. (3):

$$Q = W_Q F_{\text{SAR}}, \quad K = W_K F_{\text{Optical}}, \quad V = W_V F_{\text{Optical}} \quad (3)$$

where  $W_Q, W_K, W_V$  are learnable parameters. Scaled dot-product attention is then used to compute inter-source correlation weights (Eq. (4)):

$$A = \text{Softmax} \left( \frac{QK^\top}{\sqrt{d}} \right) \quad (4)$$

These weights are applied to reweight the optical features, producing fused multi-source features (Eq. (5)):

$$F_{\text{cross}} = F_{\text{SAR}} + A \cdot V \quad (5)$$

This mechanism retains the sensitivity of SAR to vegetation structure and water content, while adaptively incorporating optical spectral and phenological information, thereby enhancing feature discriminability. By applying the attention fusion at multiple hierarchical levels, P\_SVCN dynamically adjusts the contribution of each source, effectively distinguishing vegetation types with similar spectral properties but differing temporal and salinity–hydrology conditions.

To fully exploit the advantages of multiple attention mechanisms, the SAR–Optical Cross-Source (SOCS) block employs three parallel attention operations along the channel dimension: window attention (WA), shifted window attention (SWA), and long-range attention (LRA) (Song and Zhong, 2022). For an input feature map  $T_i \in \mathbb{R}^{H \times W \times C}$ , the channels are evenly split into  $K = 3$  groups, each processed by one of the three attention mechanisms. Let the group feature dimensions be  $x^{(1)}, x^{(2)}, x^{(3)}$ , satisfying  $x^{(1)} + x^{(2)} + x^{(3)} = C$ . Each group is input to its respective attention module, and the outputs are concatenated along the channel dimension, forming the SOCS block output:

$$\text{SOCS}(T_i) = \text{Conv}_{1 \times 1} \left( \text{CAT}(\text{WA}(x^{(1)}), \text{SWA}(x^{(2)}), \text{LRA}(x^{(3)})) \right) \quad (6)$$

where  $\text{WA}(\cdot)$ ,  $\text{SWA}(\cdot)$ , and  $\text{LRA}(\cdot)$  denote window attention, shifted window attention, and long-range attention, respectively, and  $\text{CAT}(\cdot)$  represents channel-wise concatenation.

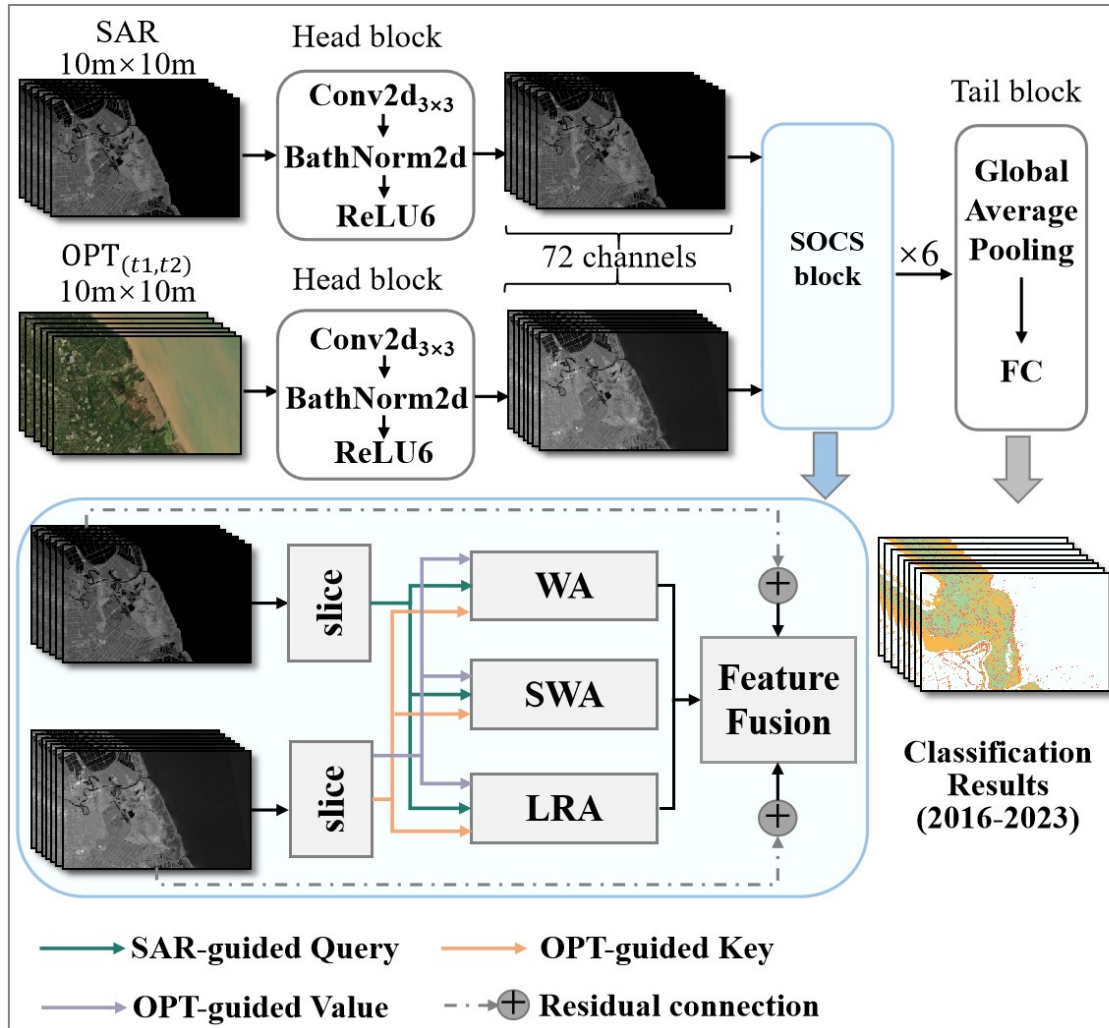


**Figure 3. Architecture of our proposed model, P\_SVCN.** The network has dual branches for Sentinel-1 SAR and dual-phase Sentinel-2 optical imagery. Each branch begins with a Head Block producing 72-channel features. Features pass through six SOCS blocks with window attention, shifted window attention, and long-range attention, residual connections, and feature fusion. Fused features are pooled globally and fed to a fully connected layer for classification, producing coastal wetland vegetation maps (2016–2023).

#### 205 3.4.4 Model Training and Implementation Details

The proposed P\_SVCN framework was implemented using the PyTorch deep learning library and trained on an NVIDIA GeForce RTX 4090 GPU. To optimize the network parameters for the classification of six coastal wetland vegetation types, we employed the Adam optimizer (Kingma and Ba, 2015) with a weight decay of  $1 \times 10^{-5}$  to provide regularization and enhance generalization. The initial learning rate was set to  $1 \times 10^{-4}$ , and the epsilon parameter ( $\epsilon$ ) for numerical stability was maintained at  $1 \times 10^{-8}$ .

To ensure stable convergence and prevent the model from becoming trapped in local optima during the fine-grained classification of multi-source Sentinel-1/2 data, a MultiStepLR scheduler was utilized. The learning rate was decayed by a factor of 0.1 ( $\gamma = 0.1$ ) at specified milestones, specifically at epochs 30, 60, and 90. The Cross-Entropy loss function was adopted as the objective function to minimize categorical errors across the six classes. The entire training process spanned 100 epochs with a mini-batch size of 32.

#### 3.4.5 Accuracy evaluation of P\_SVCN

To evaluate the classification performance of the proposed P\_SVCN, an independent accuracy assessment was conducted. All samples were randomly divided into training and validation subsets in a strict 7:3 ratio to ensure a balanced representation of vegetation classes, with 4,668 in situ data points used for model validation.

Model performance was evaluated using a confusion matrix, from which several widely adopted statistical metrics were derived, including Overall Accuracy (OA), Producer's Accuracy (PA), User's Accuracy (UA), F1-score, and the Kappa coefficient (Morales-Barquero et al., 2019). Specifically, the Overall Accuracy (OA), representing the proportion of correctly classified samples among all validation samples, was computed as shown in Eq. (7). The Producer's Accuracy (PA) and User's Accuracy (UA), which quantify omission and commission errors for each class, respectively, were calculated according to Eq. (8). The F1-score, providing a harmonic mean of precision and recall for each class, was computed as in Eq. (9). Finally, the Kappa coefficient, which evaluates the agreement between the classified and reference data beyond random chance, was calculated following Eq. (10).

$$OA = \frac{\sum_{i=1}^N n_{ii}}{\sum_{i=1}^N \sum_{j=1}^N n_{ij}} \quad (7)$$

$$PA_i = \frac{n_{ii}}{\sum_{j=1}^N n_{ij}}, \quad UA_i = \frac{n_{ii}}{\sum_{j=1}^N n_{ji}} \quad (8)$$

$$F1_i = 2 \times \frac{PA_i \times UA_i}{PA_i + UA_i} \quad (9)$$

$$\kappa = \frac{p_o - p_e}{1 - p_e}, \quad p_e = \frac{\sum_{i=1}^N \left( \sum_{j=1}^N n_{ij} \right) \left( \sum_{j=1}^N n_{ji} \right)}{\left( \sum_{i=1}^N \sum_{j=1}^N n_{ij} \right)^2} \quad (10)$$

To further validate the effectiveness of the multi-source attention fusion design, P\_SVCN was compared with the Salt marsh Vegetation Classification Network (SVCN) (Li et al., 2024b), a baseline model built upon MobileNet V3. Both models were trained and validated using the same dataset and experimental settings to ensure a fair and reliable comparison. All accuracy metrics were computed in a Python environment using the scikit-learn library. This validation framework provides a systematic and objective basis for quantitatively assessing the advantages of the P\_SVCN over single-source approaches in salt marsh vegetation classification.

## 4 Results

### 4.1 CCAV-10m dataset

We present CCAV-10m, an annual 10 m resolution vegetation dataset that accurately captures the spatiotemporal dynamics of coastal wetland species across eastern China from 2016 to 2023. The dataset has a spatial resolution of 10 m and represents the first publicly released annual time series of coastal wetland vegetation in eastern China. CCAV-10m distinguishes six representative coastal wetland vegetation types—*S. alterniflora*, *P. australis*, *Suaeda spp.*, *S. mariqueter*, mangroves, and *T. chinensis*—achieving species-level classification. Model validation shows a high overall accuracy (OA) of 0.916 and a Kappa coefficient of 0.898, indicating stable and reliable identification across all vegetation types.

In 2023, coastal wetlands in eastern China covered a total area of 617,976.38 ha, comprising six dominant vegetation types: *S. alterniflora*, *P. australis*, *Suaeda spp.*, *S. mariqueter*, *T. chinensis*, and mangroves (Fig. 4). From 2016 to 2023, coastal wetland vegetation exhibited pronounced interannual dynamics across eastern China (Tab. 2), with *Suaeda spp.* as the dominant type, followed by *S. alterniflora*, whose coverage is nearly equivalent to the combined extent of *P. australis*, mangroves, *S. mariqueter*, and *T. chinensis*. *S. alterniflora*, as an invasive saltmarsh species, maintained a relatively stable area, fluctuating between 20,202 ha and 25,918 ha, with occasional declines. *Suaeda spp.* showed a notable increasing trend, expanding from 24,436 ha in 2018 to 35,452 ha in 2023. *P. australis* exhibited considerable interannual variability, reaching its maximum of 22,893 ha in 2020, then decreasing to 10,614 ha in 2023. *T. chinensis* and *S. mariqueter* occupied relatively smaller areas, although *T. chinensis* experienced localized expansion in 2020 and 2022. As a key component of coastal protection, mangroves increased from 4,894 ha in 2017 to 7,648 ha in 2023, showing an overall upward trend.

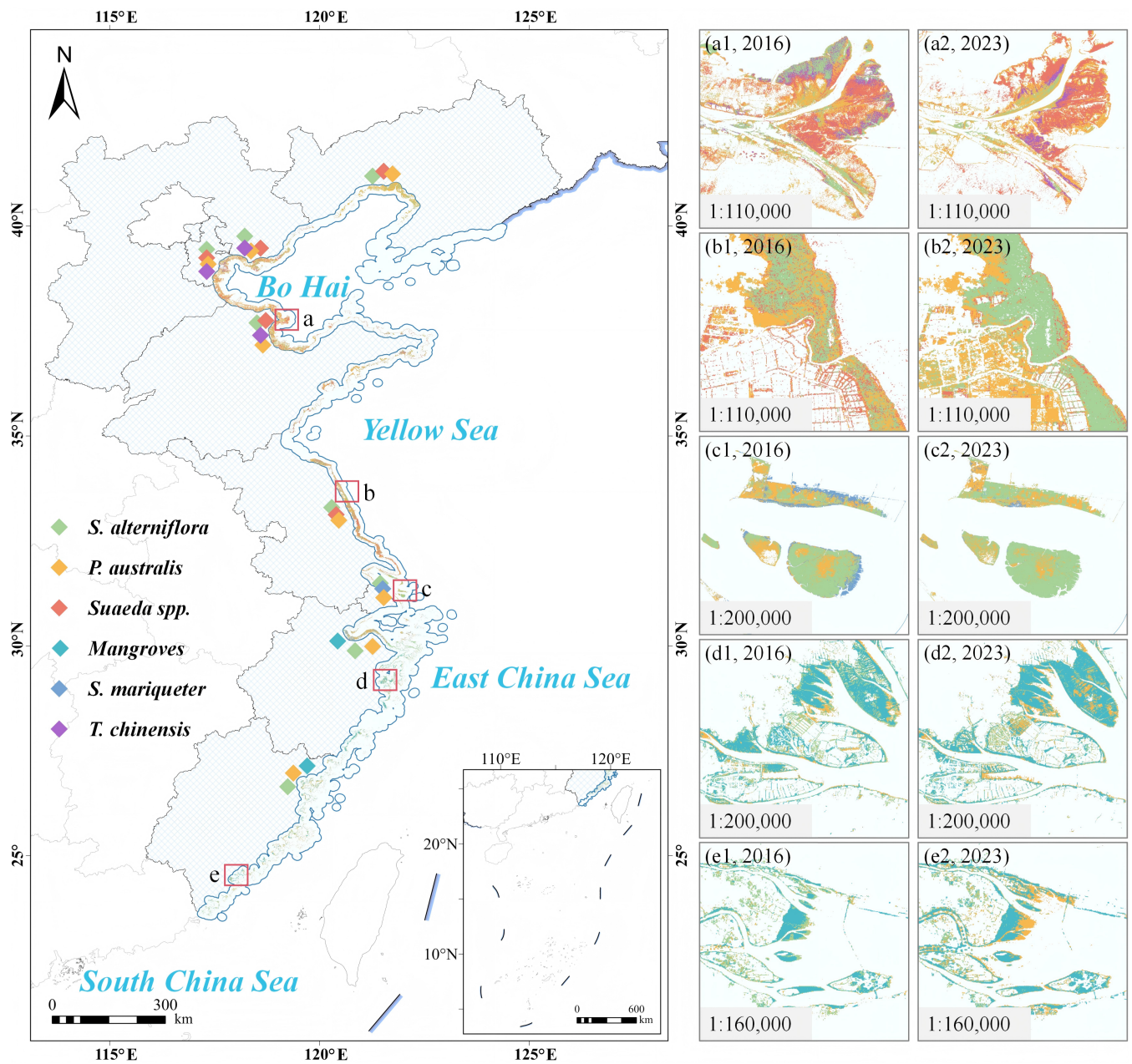


**Figure 4. Spatial distribution of coastal wetland vegetation in eastern China and representative regional changes from 2016 to 2023.** The main map shows the distribution of dominant coastal wetland species across eastern China in 2023. Insets illustrate the temporal changes in species distribution for key coastal regions: (a1, 2016) and (a2, 2023) represent the Yellow River Estuary; (b1, 2016) and (b2, 2023) represent the Jiangsu coast; (c1, 2016) and (c2, 2023) represent the Yangtze River Estuary; (d1, 2016) and (d2, 2023) represent the Zhejiang coast; and (e1, 2016) and (e2, 2023) represent the Fujian coast.

**Table 2. Area of coastal wetland vegetation types in eastern China from 2016 to 2023 (ha).** The table summarizes annual changes for six representative vegetation types (*S. alterniflora*, *Suaeda spp.*, *P. australis*, *T. chinensis*, *S. mariqueter*, and mangroves), highlighting temporal dynamics and trends over the eight years.

Vegetation Type	2016	2017	2018	2019	2020	2021	2022	2023
<i>S. alterniflora</i>	23218	25918	22855	20202	22952	20201	22970	22384
<i>Suaeda spp.</i>	30670	27149	24436	25819	28567	32087	27484	35452
<i>P. australis</i>	10711	11772	10171	16349	22893	15411	15233	10614
<i>T. chinensis</i>	1161	2063	1159	1320	3173	2502	3449	2085
<i>S. mariqueter</i>	3913	4046	3019	3551	2708	2923	2203	2270
mangroves	5320	4894	5293	6203	7898	7030	6630	7648

The transition matrices (Fig. 5) derived from the classification results of 2016, 2018, 2020, and 2023 indicate that the dominant wetland vegetation types along the coast of eastern China experienced substantial dynamics during this period. Overall, transitions among *S. alterniflora*, *Suaeda spp.*, and *P. australis* were the most frequent, whereas the distributions of *T. chinensis*, *S. mariqueter*, and mangroves remained relatively stable.

260 During 2016–2018, the primary transitions occurred from *Suaeda spp.* and *P. australis* to *S. alterniflora*, with transition areas of approximately 830 ha (30.5%) and 2,800 ha (26.0%), respectively. The self-persistence of *S. alterniflora* was about 7,970 ha (56.6%), higher than that of other types, indicating that most patches maintained their type between the two periods. In 2018–2020, these transitions intensified, with areas converting from *Suaeda spp.* and *P. australis* to *S. alterniflora* reaching approximately 560 ha (17.0%) and 2,910 ha (23.5%), respectively, both higher than in the previous period. The net gain of  
265 *S. alterniflora* during this interval was about 3,810 ha, representing the most pronounced expansion phase, consistent with its large-scale colonization of the lower tidal flats. During 2020–2023, the overall transition rate decreased. The reverse transitions from *S. alterniflora* to *Suaeda spp.* and *P. australis* were approximately 970 ha (8.2%) and 3,520 ha (29.6%), respectively, while conversions from *Suaeda spp.* to *S. alterniflora* still accounted for 1,720 ha (25.1%), suggesting local replacement or management interventions. The areas of change for mangroves and *T. chinensis* were both less than 200 ha (<1%), remaining  
270 concentrated in the southern estuarine regions.

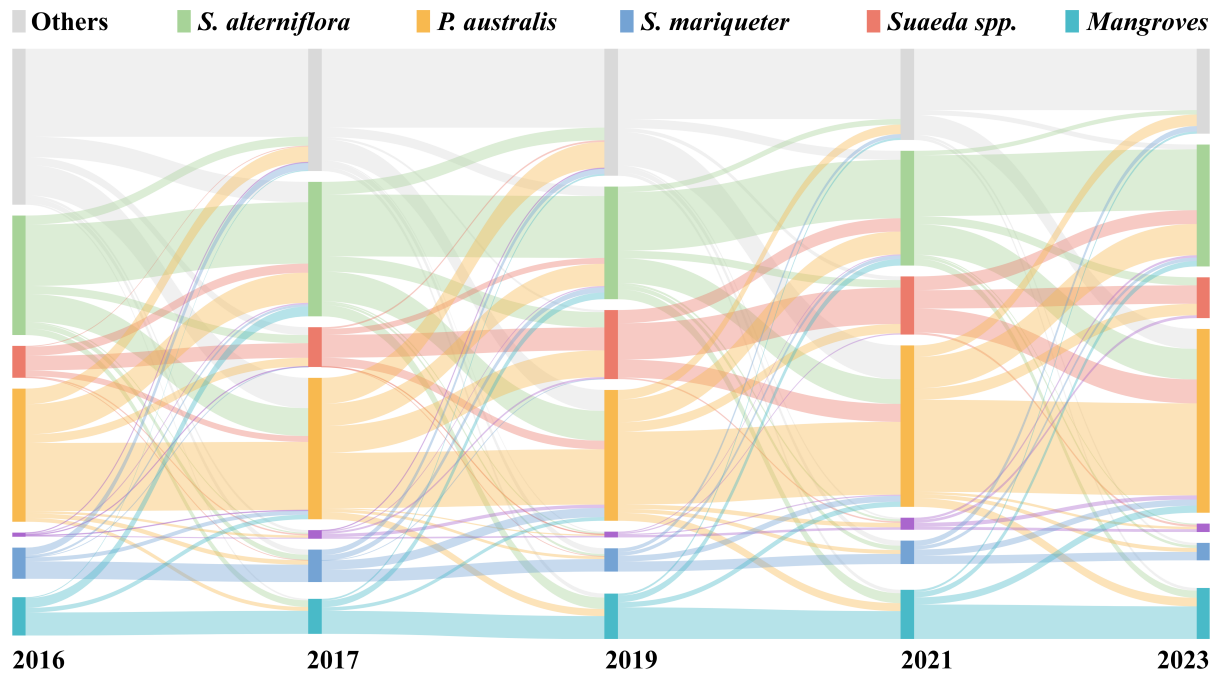


**Figure 5.** Sankey diagram showing the transitions among coastal wetland vegetation types in eastern China from 2016 to 2023. The width of each flow represents the area of vegetation conversion between consecutive years, highlighting dominant succession pathways and interannual dynamics among *S. alterniflora*, *Suaeda spp.*, *P. australis*, *T. chinensis*, *S. mariqueter*, and mangroves.

#### 4.2 Performance evaluation of P\_SVCN

A total of 15,558 in-situ data points were collected across eastern China's coastal wetlands and partitioned into training (70%) and validation (30%,  $n = 4,668$ ) sets following a stratified random sampling principle based on both vegetation types and geographic regions. To further evaluate the effectiveness of the proposed P\_SVCN model, we compared its performance with the Salt marsh Vegetation Classification Network (SVCN) (Li et al., 2024b) on the same validation dataset. As shown in Tab. 3, P\_SVCN outperformed SVCN across all vegetation classes. For *S. alterniflora*, P\_SVCN achieved a producer's accuracy (PA) of 0.927, user's accuracy (UA) of 0.882, and F1 score of 0.904, compared to 0.881, 0.820, and 0.849 for SVCN. For *P. australis*, the corresponding values were 0.921, 0.880, and 0.900 for P\_SVCN versus 0.876, 0.829, and 0.852 for SVCN. For *Suaeda spp.*, P\_SVCN yielded a PA of 0.904, UA of 0.954, and F1 score of 0.928, higher than SVCN (PA = 0.851, UA = 0.920, F1 = 0.884). Similarly, *S. mariqueter* (P\_SVCN: 0.937/0.953/0.945; SVCN: 0.902/0.927/0.914), mangroves (P\_SVCN: 0.918/0.979/0.948; SVCN: 0.890/0.953/0.921), and *T. chinensis* (P\_SVCN: 0.846/0.813/0.829; SVCN: 0.811/0.796/0.803) also exhibited higher accuracy metrics under P\_SVCN. The overall accuracy (OA) and Kappa coefficient for P\_SVCN were 0.916 and 0.898, respectively, exceeding those of SVCN (OA = 0.874, Kappa = 0.845). These results indicate that the dual-branch multi-source attention design of P\_SVCN effectively enhances classification performance for coastal wetland vegetation types.

**Table 3. Comparison of classification accuracy between P\_SVCN and SVCN for coastal wetland vegetation types.** The upward arrow (↑) indicates that the P\_SVCN’s metric values are comparatively higher, demonstrating the P\_SVCN’s superior performance.

Vegetation Type	P_SVCN (this study)↑			SVCN (Li et al., 2024b)		
	PA↑	UA↑	F1↑	PA	UA	F1
<i>S. alterniflora</i>	0.927	0.882	0.904	0.881	0.820	0.849
<i>P. australis</i>	0.921	0.880	0.900	0.876	0.829	0.852
<i>Suaeda spp.</i>	0.904	0.954	0.928	0.851	0.920	0.884
<i>S. mariqueter</i>	0.937	0.953	0.945	0.902	0.927	0.914
mangroves	0.918	0.979	0.948	0.890	0.953	0.921
<i>T. chinensis</i>	0.846	0.813	0.829	0.811	0.796	0.803
Overall Accuracy (OA)	0.916			0.874		
Kappa	0.898			0.845		

285 The detailed confusion matrices for the P\_SVCN and SVCN models are presented in Fig. 6. Rows correspond to the ground truth classes, and columns represent predicted classes. Diagonal entries indicate the number of correctly classified samples, while off-diagonal elements reflect misclassifications. P\_SVCN shows consistently higher per-class accuracy compared with SVCN. The largest improvements are observed in *Suaeda spp.* and *T. chinensis*, which are often confused with neighboring species in SVCN predictions. Misclassifications in both models mainly occur between spectrally or structurally similar vegetation types, such as *S. alterniflora* vs. *P. australis*. This highlights the advantage of P\_SVCN’s multi-source feature integration, which effectively captures both SAR structural information and optical phenology for improved discriminability.

290 This marked performance leap is fundamentally attributed to the synergistic integration of multi-temporal optical phenology and Synthetic Aperture Radar (SAR) structural attributes within the P\_SVCN architecture. In contrast to the SVCN model, which relies exclusively on Sentinel-1 SAR backscattering coefficients ( $\sigma^0$ ), P\_SVCN introduces multi-temporal optical observations to construct a high-dimensional Phenological-Spectral Vector (PSV).

295 Within complex coastal wetland ecotones, discriminating between vegetation species with analogous physical architectures is inherently constrained when relying solely on SAR observations. Furthermore, radar backscatter is highly susceptible to fluctuations in the surface dielectric constant induced by periodic tidal inundation. P\_SVCN effectively circumvents the information bottleneck of single-source radar data by utilizing the PSV to characterize species-specific growth trajectories—most notably the distinctive "red beach" spectral signature of *Suaeda spp.* during the senescence stage (Phase 2). Simultaneously, the framework preserves the deterministic advantages of SAR in characterizing canopy volume and biomass. By leveraging a multi-source attention mechanism, P\_SVCN facilitates dynamic complementarity between the optical "biological fingerprint" and the radar-derived "physical structure," thereby substantially mitigating classification uncertainty.

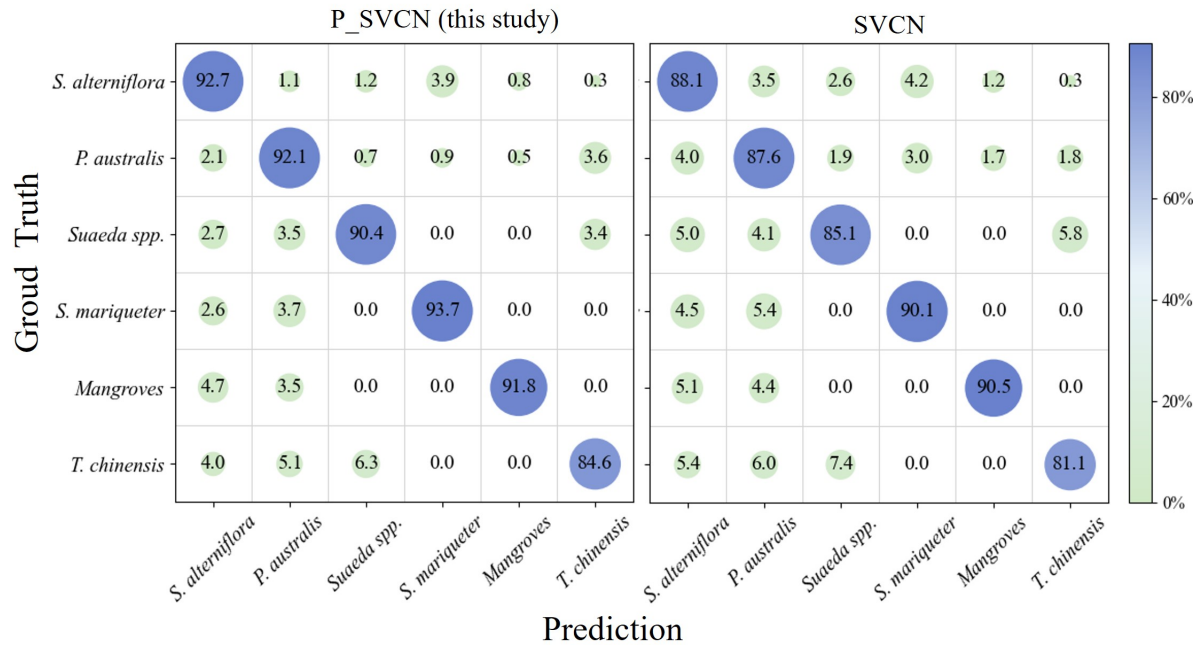


**Figure 6. Comparison of confusion matrices for P\_SVCN and SVCN on coastal wetland vegetation classification.** The diagonal elements indicate the percentage of correctly classified samples, while the off-diagonal elements represent the percentage of misclassified samples.

## 5 Discussion

### 305 5.1 The CCAV-10m dataset: Filling a critical gap in coastal wetland vegetation mapping

We introduce CCAV-10m, an annual 10m coastal wetland vegetation dataset generated using the P-SVCN model, which captures the spatial and temporal dynamics of eastern coastal China’s wetland vegetation from 2016 to 2023. As the first publicly available species-level coastal wetland dataset for this region, CCAV-10m provides fine-resolution mapping of six representative vegetation types—*S. alterniflora*, *P. australis*, *Suaeda spp.*, *S. mariqueter*, mangroves, and *T. chinensis*. Model evaluation  
310 demonstrates robust performance, with an overall accuracy of 0.916 and a Kappa coefficient of 0.898.

Compared with existing coastal wetland datasets (Table 4), CCAV-10m demonstrates significant advantages in terms of spatial coverage, functional composition, and temporal continuity. First, regarding spatial coverage, CCAV-10m spans the entire coastal zone of eastern China, and its 10 m resolution enables precise delineation of complex intertidal vegetation mosaics. In contrast, SaltMarshVegYRD (Zhang et al., 2021) is limited to the Yellow River Delta with a 30 m resolution, and CMSA (Li  
315 et al., 2024a), although also at 10 m resolution, focuses solely on a single invasive species, failing to systematically represent coastal vegetation patterns at the national scale. Second, in terms of functional composition, CCAV-10m provides species-level refinement, differentiating six representative vegetation types along the Chinese coast: *S. alterniflora*, *P. australis*, *Suaeda*

*spp.*, *S. mariqueter*, mangroves, and *T. chinensis*. By comparison, CCSV(Zhao et al., 2023) classifies only broad salt marsh categories, and CMSA focuses exclusively on the invasive species *S. alterniflora*, both lacking intra-community functional differentiation. Finally, in the temporal dimension, CCAV-10m offers a continuous annual time series from 2016 to 2023, enabling long-term and systematic monitoring of coastal wetland dynamics. In contrast, CCSV contains only a single epoch in 2020, and CMSA provides annual sequences but only for a single species.

CCAV-10m achieves multidimensional improvements in spatial coverage, functional composition, and temporal continuity. It represents the first high-resolution coastal vegetation dataset in eastern China with multi-species recognition and annual consistency, providing unified and high-quality baseline data for studies on coastal ecosystem succession, invasive species spread, and blue carbon assessment.

**Table 4. Comparison of CCAV-10m with existing coastal wetland datasets.**

Dataset	Spatial Coverage	Spatial Resolution	Functional Composition	Temporal Dimension
<b>CCAV-10m (Ours)</b>	Eastern China's Coastal Wetland	10 m	<i>S. alterniflora</i> , <i>P. australis</i> , <i>Suaeda spp.</i> , <i>S. mariqueter</i> , mangroves, <i>T. chinensis</i>	2016–2023
SaltMarshVegYRD (Zhang et al., 2021)	Yellow River Delta wetland	30 m	<i>S. alterniflora</i> , <i>P. australis</i> , <i>Suaeda spp.</i>	1999–2020
CCSV (Zhao et al., 2023)	China's Coastal Wetland	10 m	Salt marsh	2020
CMSA (Li et al., 2024a)	China's Coastal Wetland	10 m	<i>S. alterniflora</i>	2017–2021

## 5.2 Provincial-scale dynamics of eastern China's coastal wetland vegetation (2016–2023)

Coastal wetland vegetation exhibited clear provincial-scale differences in eastern China from 2016 to 2023. In Liaoning Province, the dominant vegetation types included *S. alterniflora*, *Suaeda spp.*, and *P. australis*. Hebei, Shandong, and Tianjin showed similar compositions, characterized mainly by *S. alterniflora*, *Suaeda spp.*, and *P. australis*, with additional occurrences of *T. chinensis* in specific areas. In Jiangsu Province, coastal wetlands were primarily dominated by *S. alterniflora*, *Suaeda spp.*, and *P. australis*. Shanghai featured a vegetation assemblage composed of *S. alterniflora*, *S. mariqueter*, and *P. australis*. In Zhejiang Province, *S. alterniflora* and *S. mariqueter* were widely distributed, accompanied by patches of mangroves and *P. australis*. Fujian Province, located at the southernmost part of the study area, was characterized by extensive mangrove ecosystems, with additional distributions of *S. alterniflora* and *P. australis*.

Coastal wetlands showed clear provincial differences in area and species composition (Fig. 7). Jiangsu, Shandong, and Zhejiang had the largest wetland areas, followed by Fujian, Liaoning, and Shanghai, while Hebei and Tianjin were smaller. *S. alterniflora* and *P. australis* dominated most provinces, with *Suaeda spp.*, *T. chinensis*, *S. mariqueter*, and mangroves restricted but ecologically important. In Liaoning, wetlands were stable, dominated by *P. australis* (450–530 ha) and *S. alterniflora* (450–9,030 ha). Tianjin had scattered wetlands (400–780 ha) with alternating dominance of *P. australis* and *Suaeda spp.*. Hebei showed pronounced species dynamics, with *S. alterniflora* stable (1,320–2,420 ha) and *P. australis* increasing from 2,870 to 3,730 ha. Shandong experienced significant changes, *P. australis* rising from 3,910 to 7,120 ha, reflecting *Spartina* control effects. Jiangsu, the largest coastal wetland province, had over 60% combined *S. alterniflora* and *P. australis*, with *P. australis* slightly increasing from 3,740 to 4,710 ha. In Shanghai, wetlands shrank from 1,300 to 970 ha, while *S. mariqueter* partially recovered post-2021. Zhejiang’s wetlands alternated between *S. alterniflora* and *P. australis* (2,990–5,240 ha), and *S. mariqueter* remained stable (2,110–4,210 ha). Fujian’s wetlands were relatively stable (2,290–3,850 ha), dominated by *S. alterniflora*. Detailed annual values for each province and species are provided in the Appendix A (Table A1). Coastal wetlands exhibited clear provincial differences, with *S. alterniflora* and *P. australis* dominating most regions, while *Suaeda spp.*, *T. chinensis*, *S. mariqueter*, and mangroves were more restricted in distribution yet remained ecologically significant, reflecting localized dynamic adjustments within a generally stable vegetation structure.

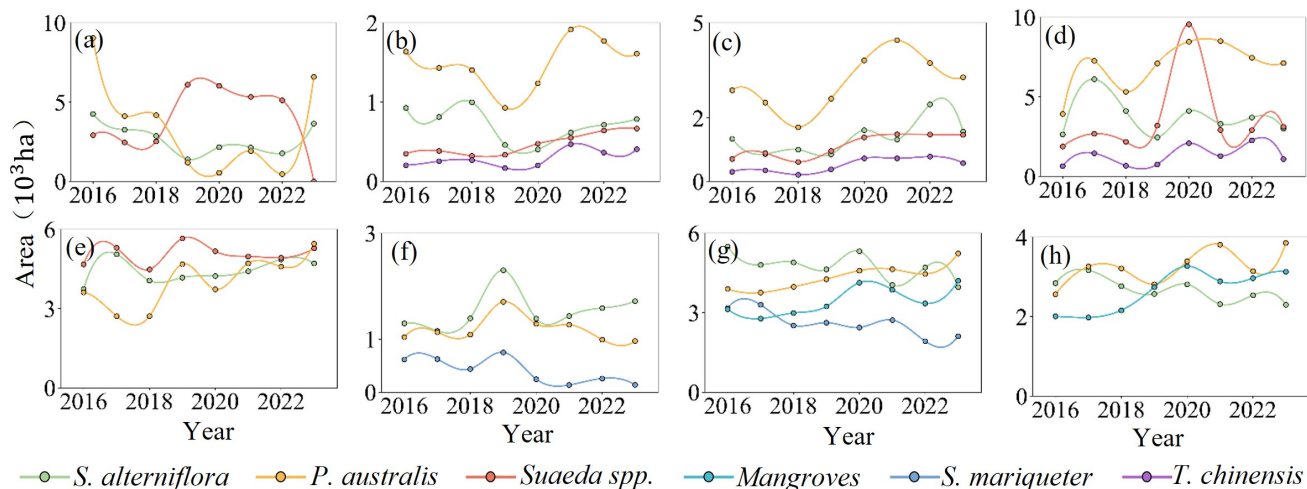


**Figure 7. Temporal dynamics of wetland vegetation area in eight Chinese coastal provinces from 2016 to 2023.** (a) Liaoning, (b) Tianjin, (c) Hebei, (d) Shandong, (e) Jiangsu, (f) Shanghai, (g) Zhejiang, and (h) Fujian.

### 5.3 Uncertainty analysis of the CCAV-10m dataset

Despite the high overall classification accuracy of the CCAV-10m dataset (OA = 0.916), certain uncertainties remain (Tab. 5). To quantitatively evaluate potential sources of error, we conducted ablation experiments comparing three input configurations: Sentinel-1 only (S1), Sentinel-2 only (S2, dual-temporal composite), and the S1+S2 fusion mode. The overall accuracies were

355 0.895, 0.870, and 0.916, respectively, indicating significant complementarity between radar and optical information in intertidal wetland vegetation identification.

From the classification results, the S1-only configuration slightly outperformed S2 in most vegetation types, particularly in the discrimination of *S. alterniflora* and *P. australis*. Sentinel-1 C-band SAR captures canopy structure, surface roughness, and moisture scattering features (Zhang et al., 2022a; Mleczko and Mróz, 2018; Rajngewerc et al., 2022), which are less sensitive to  
360 optical disturbances caused by turbid water and cloudy conditions, thus providing advantages in identifying structurally distinct vegetation. In contrast, the S2-only configuration, although leveraging dual-temporal imagery to enhance spectral temporal information, is affected by surface albedo variations and spectral mixing in intertidal zones (Feng et al., 2022), resulting in misclassifications between spectrally similar types such as *Suaeda spp.* and *T. chinensis*. The S1+S2 fusion significantly improved per-class producer's accuracy (PA) and user's accuracy (UA), effectively mitigating the limitations of single data  
365 sources. The structural and moisture information from SAR complements the spectral and vegetation index features from optical imagery, enabling stable model performance across different tidal stages and climatic conditions, particularly enhancing the separability of *Suaeda spp.* and *T. chinensis*.

Nevertheless, residual uncertainties persist. First, *T. chinensis* and *Suaeda spp.* are often interspersed in the upper wetland, with similar temporal and phenological characteristics (Gao et al., 2015; Jiao et al., 2021; Wu et al., 2020), making complete  
370 discrimination challenging even under multi-source fusion. Second, *S. mariqueter* has a narrow and highly patchy distribution (Gu et al., 2021), which may result in omission errors under 10 m resolution. Third, despite the overall robustness of the model, localized "out-of-range" misclassifications were observed (e.g., mangrove patches erroneously identified in Hangzhou Bay, exceeding their northern distribution limit).

Future studies could integrate higher-resolution SAR data (e.g., TerraSAR-X, GF-3) and incorporate geographic prior knowl-  
375 edge—such as latitudinal distribution limits and climatic thresholds—as spatial constraints in the post-processing phase. Such a knowledge-guided approach will effectively filter out biologically inconsistent errors and further enhance the spatial reliability of coastal wetland mapping.

**Table 5. Comparison of producer’s accuracy (PA) and user’s accuracy (UA) for different input configurations: Sentinel-1 (S1), Sentinel-2 (S2, dual-temporal), and S1+S2 fusion.** The upward arrow (↑) indicates that the S1+S2 configuration achieves comparatively higher metric values, demonstrating its superior performance.

Class	PA (S1)	PA (S2)	PA (S1+S2)↑	UA (S1)	UA (S2)	UA (S1+S2)↑
<i>S. alterniflora</i>	0.913	0.887	0.927	0.859	0.879	0.882
<i>P. australis</i>	0.898	0.868	0.921	0.853	0.857	0.880
<i>Suaeda spp.</i>	0.883	0.852	0.904	0.939	0.842	0.954
<i>S. mariqueter</i>	0.924	0.901	0.937	0.943	0.891	0.953
<i>Mangroves</i>	0.891	0.851	0.918	0.975	0.837	0.979
<i>T. chinensis</i>	0.800	0.762	0.846	0.747	0.782	0.813
Overall Accuracy (OA)	0.895	0.870	0.916	-	-	-

#### 5.4 Limitations of the CCAV-10m dataset

While the CCAV-10m dataset demonstrates high overall thematic fidelity, localized inter-annual fluctuations in species distribution (as illustrated in Fig. 7) necessitate a rigorous interpretation within the context of complex environmental background fields. The spatial distribution and spectral identification of coastal wetland vegetation are profoundly influenced by tidal regimes, salinity gradients, and phenological dynamics (Murray et al., 2022). Tidal inundation typically attenuates reflectance in the near-infrared (NIR) spectrum, frequently leading to the omission of low-stature vegetation due to water-induced signal absorption (Kearney et al., 2009). Simultaneously, spatial variations in salinity gradients can alter the biophysical parameters of *P. australis*, inducing localized spectral deviations that exacerbate the risk of confusion with invasive species such as *S. alterniflora* (Zhou et al., 2021; Cingano et al., 2025).

A prominent case study is the observed abrupt fluctuations of *P. australis* and *Suaeda spp.* along the Liaoning coast between 2022 and 2023. Meteorological back-analysis reveals that these shifts are not indicative of actual ecological succession but are instead "environmental artifacts" induced by extreme hydrometeorological anomalies. From August to September 2023, the Liaoning coastal zone was struck by the consecutive impacts of Typhoons Doksuri and Khanun, which triggered rare and catastrophic precipitation events (Service, 2023).

This extreme climate directly compromised the classification logic through two primary mechanisms. First, the physical submergence and subsequent spectral masking. Since *Suaeda spp.* is a low-stature species with a typical height of less than 30 cm, it is highly susceptible to complete submergence by typhoon-induced storm surges and inland flooding. During the critical "red beach" phenological window in 2023, record-breaking rainfall caused widespread surface water pooling. The regional mean NDWI increased from -0.041 in 2022 to -0.029 in 2023, confirming a significant intensification of the moisture signal (Fig. 8b). This hydrological stress led to strong NIR absorption by the overlying water, which severely dampened the diagnostic

spectral signatures of the vegetation and reduced the Signal-to-Noise Ratio (SNR). Consequently, the extracted phenological profiles underwent major distortions that resulted in localized omission errors.

400 Second, the interplay between atmospheric constraints and observation gaps. The persistent storm systems associated with these typhoons triggered a surge in regional cloudiness. Mean cloud cover during the two critical phases reached 50.76% and 41.25% respectively (Fig. 8a). Although we maintained a 10% cloud-cover threshold for scene selection, the sheer frequency of cloudy days in 2023 drastically curtailed the availability of high-quality "clear-sky" pixels during the peak phenological stages. This scarcity forced a reliance on temporally offset or sub-optimal observations, which hindered the capacity of the  
405 model to accurately reconstruct fine-scale phenological trajectories (Cingano et al., 2025). As a result, the distinctive spectral contrast of coastal vegetation was partially compromised by increased atmospheric noise and reduced observation frequency.

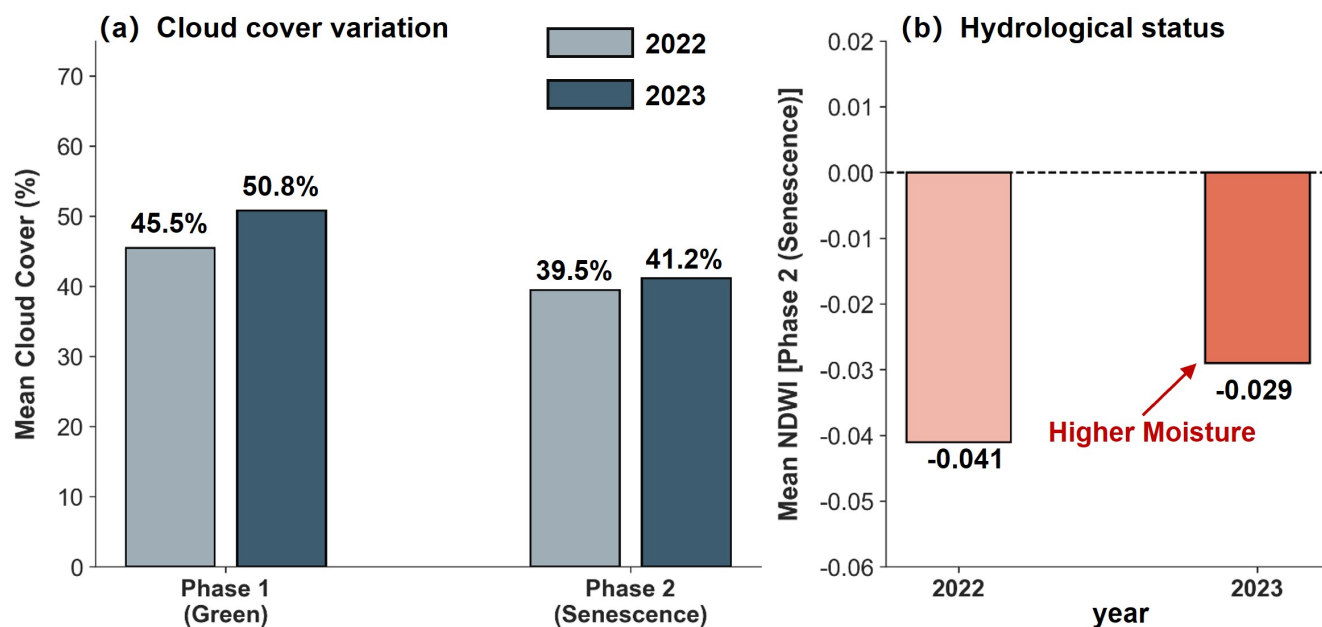


**Figure 8. Comparative analysis of environmental constraints in the Liaoning coastal zone (2022–2023).** (a) Atmospheric Constraints: Mean cloud cover (%) during the green (Phase 1) and senescence (Phase 2) stages. (b) Hydrologic Signal: Mean Normalized Difference Water Index (NDWI) during Phase 2 (senescence).

The CCAV-10m dataset possesses inherent limitations during climatically anomalous years, where the "observable area" may deviate from the "actual distribution" due to environmental noise. Future iterations of the CCAV-10m framework will prioritize the integration of SAR-derived inundation masks and multi-source high-frequency data fusion to effectively decouple  
410 ecological evolutionary signals from short-term environmental noise within complex coastal ecotones.

## 6 Conclusions

This study developed a phenology-guided coastal wetland vegetation classification network integrating Sentinel-1/2 (P\_SVCN) and generated the CCAV-10m dataset, which maps the wetland vegetation types in eastern coastal China from 2016 to 2023. By integrating multi-source Sentinel-1 SAR and Sentinel-2 MSI data, the P\_SVCN fully exploits structural and phenological features, enabling accurate discrimination of spectrally similar and spatially fragmented vegetation types. The results are summarized as follows:

(1) A long-term, high-resolution species-level vegetation dataset (CCAV-10m). The dataset provides annual species-level maps of coastal wetland vegetation at a spatial resolution of 10 m, distinguishing six dominant plant types. Spatiotemporal analysis shows that *Suaeda spp.* is the predominant vegetation type, followed by *S. alterniflora*, whose coverage nearly matches the combined extent of *P. australis*, mangroves, *S. mariqueter*, and *T. chinensis*. Further temporal assessments reveal pronounced community succession in recent years, including the continued expansion of *S. alterniflora* and *Suaeda spp.*, fluctuating patterns in *P. australis*, and a steady increase in mangrove extent. Transition matrices indicate that conversions among *S. alterniflora*, *Suaeda spp.*, and *P. australis* occurs most frequently, reflecting the dynamic responses of coastal wetland ecosystems to natural processes and human activities.

(2) A novel phenology-guided deep-learning framework (P\_SVCN). The P\_SVCN model exhibits strong classification performance, achieving an overall accuracy of 0.916 and a Kappa coefficient of 0.898 based on validation with 4,668 in situ samples. These results exceed those of the baseline SVCN model (overall accuracy 0.874, Kappa 0.845). Ablation experiments further demonstrate the complementary strengths of Sentinel-1 synthetic aperture radar and Sentinel-2 optical observations, particularly in distinguishing vegetation types with highly similar spectral properties or fragmented spatial patterns.

CCAV-10m effectively bridges the gap between coarse-resolution ecosystem maps and single-species products by balancing species-level classification accuracy and large-scale spatial coverage. The dataset provides high-precision spatiotemporal information for monitoring vegetation succession, assessing invasive species, estimating blue carbon stocks, and supporting ecological restoration planning. Moreover, it offers a robust foundation for sustainable coastal ecosystem management under global environmental change. The CCAV-10m dataset is publicly available at <https://doi.org/10.57760/sciencedb.31077>, supporting reproducibility and further applications in related research.

*Data availability.* The Sentinel-1 synthetic aperture radar (SAR) and Sentinel-2 multispectral data used in this study are available from the Copernicus Open Access Hub (<https://scihub.copernicus.eu>, last access: 21 October 2025) under the Copernicus open data policy. The species-level coastal wetland vegetation dataset, CCAV-10m, produced in this study is publicly available at the Science Data Bank (<https://doi.org/10.57760/sciencedb.31077>, Li et al., 2025). To ensure long-term spatiotemporal monitoring, we are committed to updating this dataset annually; these updates will be released as distinct versions corresponding to different year intervals (e.g., 2024, 2025, and beyond) and will be accompanied by updated technical documentation on the same platform. Validation samples comprising 84% of the total dataset are provided in the file ‘Vegetation samples.xlsx’ within the same repository; these samples cover all vegetation classes and major coastal

regions and were derived from field surveys, visual interpretation, and public reference sources. The remaining 16% of the field sampling data are not publicly released but can be obtained upon a reasonable scientific request to the authors.

#### 445 **Appendix A: Statistical data for provincial coastal vegetation areas**

To complement Figure 7, this appendix provides the precise numerical datasets for provincial coastal vegetation coverage. The following table organizes the annual areas ( $10^4$  ha) by province and species, covering the entire study duration from 2016 to 2023.

#### **Appendix B: Quality Control Procedures for Vegetation Samples**

##### 450 **B1 Validation of Interpretation Reliability via Field-Truth Benchmarking**

To ensure the high quality and representativeness of the training data, we implemented a rigorous validation process for our visual interpretation criteria. All interpretation was performed using high-resolution Google Earth imagery, which provides the sub-meter level detail necessary to distinguish coastal wetland vegetation.

To quantify the reliability of our interpretation criteria, we conducted a consistency verification specifically at the locations  
455 of the field-surveyed sites. In this process, interpreters were required to perform a blind identification of the vegetation types by examining the high-resolution Google Earth imagery corresponding to each field-surveyed coordinate. By cross-referencing these image-based interpretation results with the actual ground-truth observations, we calculated the Kappa coefficient ( $\kappa$ ) using Equation 10.

Our verification yielded a Kappa value of 0.95, confirming that the classification features observed on Google Earth imagery  
460 highly match the actual vegetation types on the ground.

##### **B2 Inter-Interpreter Cross-Validation**

To further mitigate subjective bias, a double-blind review process was implemented. Each sample point was independently reviewed by at least two experienced researchers. Only samples where both researchers reached a 100% consensus were retained in the final dataset. This rigorous cross-verification ensured the internal consistency and reliability of the sample pool.

465 Following the quality control and cross-verification processes, the field-surveyed data and the validated interpreted samples were integrated into a unified high-confidence dataset. To further refine the sample pool, we excluded points located in mixed pixels or transition zones to prevent spectral contamination. Finally, this refined dataset was randomly partitioned into a training set (70%) and a validation set (30%). This partitioning strategy ensures that the model is trained on reliable data while maintaining an independent set for unbiased accuracy assessment.

**Table A1.** Annual area values (10<sup>4</sup> ha) of coastal vegetation by province and species (2016–2023).

Province	Species	2016	2017	2018	2019	2020	2021	2022	2023
Fujian	<i>S. alterniflora</i>	2.84	3.16	2.76	2.57	2.81	2.31	2.53	2.29
	<i>P. australis</i>	2.56	3.26	3.21	2.81	3.39	3.80	3.14	3.85
	Mangroves	2.00	1.97	2.16	2.74	3.27	2.88	2.96	3.12
Hebei	<i>S. alterniflora</i>	1.34	0.86	1.00	0.85	1.61	1.32	2.42	1.57
	<i>Suaeda</i> spp.	0.71	0.89	0.61	0.95	1.38	1.48	1.47	1.46
	<i>P. australis</i>	2.87	2.48	1.70	2.60	3.81	4.45	3.73	3.28
	<i>T. chinensis</i>	0.30	0.34	0.21	0.37	0.73	0.72	0.78	0.57
Jiangsu	<i>S. alterniflora</i>	3.74	5.06	4.06	4.17	4.23	4.41	4.86	4.71
	<i>Suaeda</i> spp.	4.67	5.30	4.48	5.65	5.17	4.97	4.92	5.28
	<i>P. australis</i>	3.61	2.71	2.71	4.68	3.73	4.71	4.59	5.46
Liaoning	<i>S. alterniflora</i>	4.25	3.25	2.86	1.38	2.16	2.13	1.77	3.63
	<i>Suaeda</i> spp.	2.91	2.45	2.51	6.09	6.02	5.32	5.10	0.00
	<i>P. australis</i>	9.03	4.11	4.18	1.17	0.53	1.90	0.45	6.59
Shandong	<i>S. alterniflora</i>	2.63	6.10	4.10	2.44	4.10	3.29	3.69	2.99
	<i>Suaeda</i> spp.	1.87	2.67	2.16	3.19	9.55	2.90	2.90	3.11
	<i>P. australis</i>	3.91	7.26	5.31	7.09	8.46	8.49	7.45	7.12
	<i>T. chinensis</i>	0.64	1.44	0.66	0.75	2.08	1.28	2.26	1.08
Zhejiang	<i>S. alterniflora</i>	5.50	4.81	4.90	4.64	5.32	4.05	4.71	3.96
	<i>P. australis</i>	3.89	3.76	3.98	4.27	4.59	4.64	4.46	5.24
	<i>S. mariqueter</i>	3.18	3.30	2.52	2.62	2.44	2.72	1.93	2.11
	Mangroves	3.13	2.78	2.99	3.24	4.13	3.87	3.35	4.21
Tianjin	<i>S. alterniflora</i>	0.93	0.81	1.00	0.46	0.40	0.62	0.71	0.78
	<i>Suaeda</i> spp.	0.35	0.38	0.32	0.34	0.47	0.55	0.64	0.66
	<i>P. australis</i>	1.64	1.43	1.40	0.93	1.24	1.91	1.77	1.61
	<i>T. chinensis</i>	0.20	0.25	0.27	0.17	0.20	0.47	0.36	0.41
Shanghai	<i>S. alterniflora</i>	1.30	1.15	1.39	2.30	1.39	1.44	1.59	1.72
	<i>P. australis</i>	1.04	1.13	1.09	1.71	1.29	1.27	0.99	0.97
	<i>S. mariqueter</i>	0.62	0.62	0.44	0.75	0.25	0.14	0.26	0.14

## 470 Appendix C: Spatial Distribution of Samples

To ensure the transparency and reliability of the CCAV-10m dataset, we provide a visual summary of the spatial distribution of the samples used for model training and validation. A total of 15,558 samples were collected through a combination of field surveys and high-resolution manual interpretation of Google Earth.

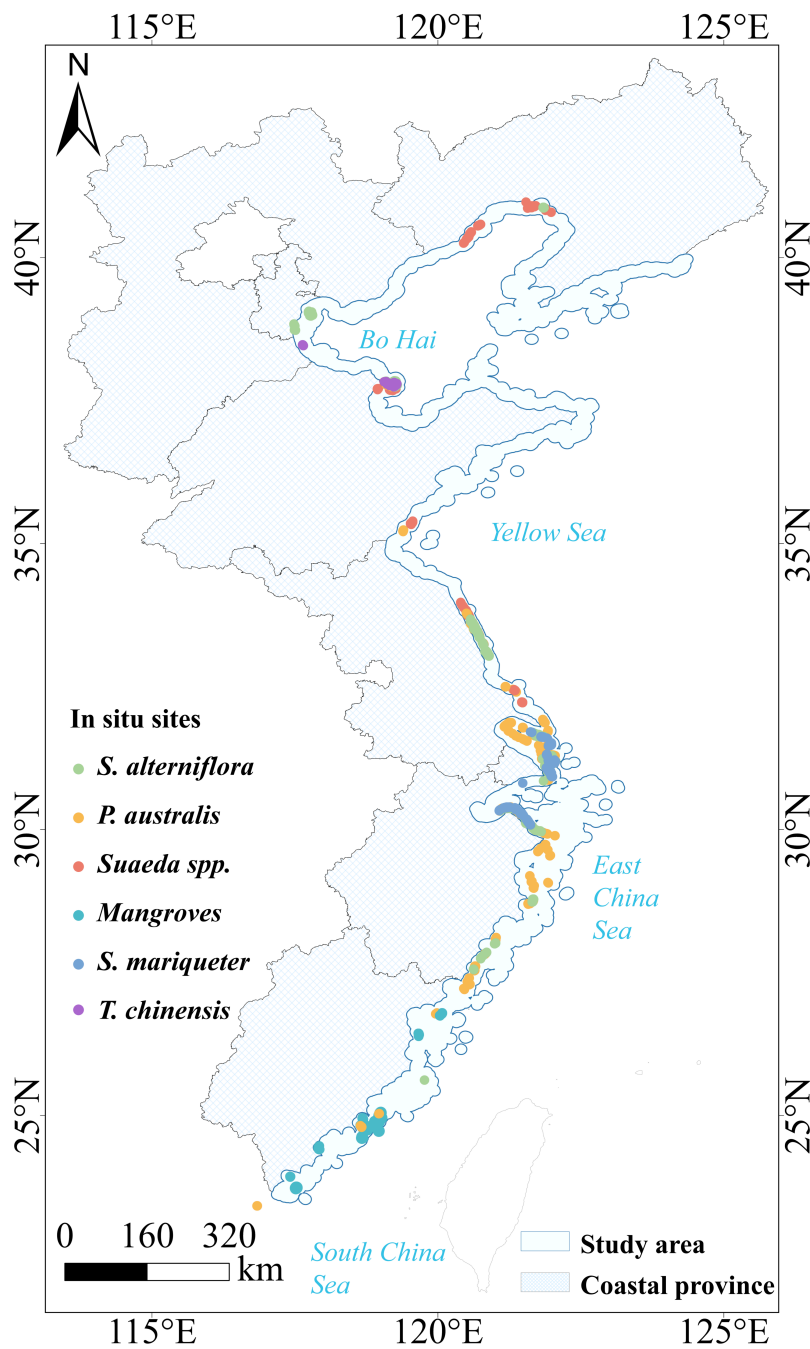


Figure C1. Spatial distribution of samples

*Author contributions.* LYY designed the research. LYY and LT performed the experiments and code. LYY wrote the manuscript. LT, SZJ, 475 YS and ZZL process data analysis. LM and YLN provided the resource. LM and YLN supervised and reviewed the manuscript.

*Competing interests.* The contact author has declared that none of the authors has any competing interests.

*Disclaimer.* To access the datasets associated with this study, users should comply with the corresponding data access policies and usage requirements. The CCAV-10m dataset is distributed under the Creative Commons Attribution 4.0 International License (CC BY 4.0).

*Acknowledgements.* This research has been supported by the National Natural Science Foundation of China (Grant No. W2412140 and 480 42230505), Open Fund of Key Laboratory of Geographic Information Science (Ministry of Education), East China Normal University (Grant No. KLGIS2025A01), and the International Research Center of Big Data for Sustainable Development Goals (Grant No. CBAS2022GSP07).

## References

- Aburto-Oropeza, O., Ezcurra, E., Danemann, G., Valdez, V., Murray, J., and Sala, E.: Mangroves in the Gulf of California increase fishery yields, *Proceedings of the National Academy of Sciences*, 105, 10456–10459, <https://doi.org/10.1073/pnas.0804601105>, 2008.
- 485 Almond, D., Chen, Y., Greenstone, M., and Li, H.: Winter heating or clean air? Unintended impacts of China's Huai river policy, *American Economic Review*, 99, 184–190, <https://doi.org/10.1257/aer.99.2.184>, 2009.
- Bao, Y., Lin, X., Jia, M., Xiao, Z., Wang, C., Liao, J., and Zhang, Y.: Convergence in key month of phenology-based mangrove species classification using sentinel-2 imagery data: insights from structural and physiological indices, *International Journal of Digital Earth*, 18, 2528–2551, <https://doi.org/10.1080/17538947.2025.2528651>, 2025.
- 490 Bernhardt, E.: Coastal freshwater wetlands squeezed between migrating salt marshes and working lands, *Science Advances*, 8, eadd1628, <https://doi.org/10.1126/sciadv.add1628>, 2022.
- Bertram, C., Quaas, M., Reusch, T. B., Vafeidis, A. T., Wolff, C., and Rickels, W.: The blue carbon wealth of nations, *Nature Climate Change*, 11, 704–709, <https://doi.org/10.1038/s41558-021-01089-4>, 2021.
- Cao, W. and Wong, M. H.: Current status of coastal zone issues and management in China: a review, *Environment International*, 33, 985–992, <https://doi.org/10.1016/j.envint.2007.04.009>, 2007.
- 495 Chen, C., Chen, Y., Liu, Z., Xue, Z., Yang, G., and Sun, W.: PCSAI: a phenological characteristics-based *Spartina alterniflora* index derived from a time-series of remote sensing images, *Big Earth Data*, pp. 1–29, <https://doi.org/10.1080/20964471.2025.2554043>, 2025.
- Chen, G., Jin, R., Ye, Z., Li, Q., Gu, J., Luo, M., Luo, Y., Christakos, G., Morris, J., He, J., et al.: Spatiotemporal mapping of salt marshes in the intertidal zone of China during 1985–2019, *Journal of Remote Sensing*, <https://doi.org/10.34133/2022/9793626>, 2022.
- 500 Chen, Y., Ebenstein, A., Greenstone, M., and Li, H.: Evidence on the impact of sustained exposure to air pollution on life expectancy from China's Huai River policy, *Proceedings of the National Academy of Sciences*, 110, 12936–12941, <https://doi.org/10.1073/pnas.1300018110>, 2013.
- Cingano, P., Moro, D., Pellegrini, E., Asquini, E., Contin, M., Trotta, G., Vuerich, M., Trevisan, F., Scagnetto, I., Casarsa, L., et al.: Integrating remote sensing and functional traits to elucidate estuarine common reed beds decline driven by soil salinity and anoxia, *Ecological Indicators*, 180, 114–129, 2025.
- 505 Costanza, R., De Groot, R., Sutton, P., Van der Ploeg, S., Anderson, S. J., Kubiszewski, I., Farber, S., and Turner, R. K.: Changes in the global value of ecosystem services, *Global environmental change*, 26, 152–158, <https://doi.org/10.1016/j.gloenvcha.2014.04.002>, 2014.
- Day, J., Anthony, E., Costanza, R., Edmonds, D., Gunn, J., Hopkinson, C., Mann, M. E., Morris, J., Osland, M., Quirk, T., et al.: Coastal wetlands in the Anthropocene, *Annual Review of Environment and Resources*, 49, 105–135, <https://doi.org/10.1146/annurev-environ-121922-041109>, 2024.
- 510 Duarte, C. M., Losada, I. J., Hendriks, I. E., Mazarrasa, I., and Marbà, N.: The role of coastal plant communities for climate change mitigation and adaptation, *Nature climate change*, 3, 961–968, <https://doi.org/10.1038/nclimate1970>, 2013.
- Feng, K., Mao, D., Qiu, Z., Zhao, Y., and Wang, Z.: Can time-series Sentinel images be used to properly identify wetland plant communities?, *GIScience & Remote Sensing*, 59, 2202–2216, <https://doi.org/10.1080/15481603.2022.2156064>, 2022.
- 515 Ferro, A., Brunner, D., Bruzzone, L., and Lemoine, G.: On the relationship between double bounce and the orientation of buildings in VHR SAR images, *IEEE Geoscience and Remote Sensing Letters*, 8, 612–616, <https://doi.org/10.1109/LGRS.2010.2097580>, 2011.
- Fu, B., Yuan, B., Yao, H., Sun, W., Jia, M., Yao, Z., and Wang, Y.: Spatio-temporal dynamics of invasive *Spartina alterniflora* and its functional traits' responding to hydro-meteorology, *Earth's Future*, 13, e2024EF005421, <https://doi.org/10.1029/2024EF005421>, 2025.

- Gabler, C. A., Osland, M. J., Grace, J. B., Stagg, C. L., Day, R. H., Hartley, S. B., Enwright, N. M., From, A. S., McCoy, M. L., and  
520 McLeod, J. L.: Macroclimatic change expected to transform coastal wetland ecosystems this century, *Nature Climate Change*, 7, 142–147,  
<https://doi.org/10.1038/nclimate3203>, 2017.
- Gallo, K., Ji, L., Reed, B., Eidenshink, J., and Dwyer, J.: Multi-platform comparisons of MODIS and AVHRR normalized difference vege-  
tation index data, *Remote Sensing of Environment*, 99, 221–231, <https://doi.org/10.1016/j.rse.2005.08.014>, 2005.
- Gao, M., Wang, X., Hui, C., Yi, H., Zhang, C., Wu, X., Bi, X., Wang, Y., Xiao, L., and Wang, D.: Assembly of plant communi-  
525 ties in coastal wetlands—the role of saltcedar *Tamarix chinensis* during early succession, *Journal of Plant Ecology*, 8, 539–548,  
<https://doi.org/10.1093/jpe/rtu037>, 2015.
- Gao, Y., Hu, Z., Wang, Z., Shi, Q., Chen, D., Wu, S., Gao, Y., and Zhang, Y.: Phenology metrics for vegetation type classification in estuarine  
wetlands using satellite imagery, *Sustainability*, 15, 1373, <https://doi.org/10.3390/su15021373>, 2023.
- Gu, J., Jin, R., Chen, G., Ye, Z., Li, Q., Wang, H., Li, D., Christakos, G., Agusti, S., Duarte, C. M., et al.: Areal extent, species composition,  
530 and spatial distribution of coastal saltmarshes in China, *IEEE Journal of Selected Topics in Applied Earth Observations and Remote  
Sensing*, 14, 7085–7094, <https://doi.org/10.1109/JSTARS.2021.3093673>, 2021.
- Gu, J., Wu, J., and Xie, D.: Coastal salt marsh changes in China: Landscape pattern, driving factors, and carbon dynamics, *Geography and  
Sustainability*, p. 100281, <https://doi.org/10.1016/j.geosus.2025.100281>, 2025.
- Hu, Y., Tian, B., Yuan, L., Li, X., Huang, Y., Shi, R., Jiang, X., Sun, C., et al.: Mapping coastal salt marshes in China using time series of  
535 Sentinel-1 SAR, *ISPRS Journal of Photogrammetry and Remote Sensing*, 173, 122–134, <https://doi.org/10.1016/j.isprsjprs.2021.01.003>,  
2021.
- Jiao, L., Zhang, Y., Sun, T., Yang, W., Shao, D., Zhang, P., and Liu, Q.: Spatial analysis as a tool for plant population conservation: A case  
study of *Tamarix chinensis* in the Yellow River Delta, China, *Sustainability*, 13, 8291, <https://doi.org/10.3390/su13158291>, 2021.
- Kang, B., Chen, X., Du, Z., Meng, W., and Li, H.: Species-based mapping of carbon stocks in salt marsh: Tianjin coastal zone as a case  
540 study, *Ecosystem Health and Sustainability*, 9, 0052, <https://doi.org/10.34133/ehs.0052>, 2023.
- Kearney, M. S., Stutzer, D., Turpie, K., et al.: The effects of tidal inundation on the reflectance characteristics of coastal marsh vegetation,  
*Journal of Coastal Research*, 25, 1177–1186, 2009.
- Kingma, D. P. and Ba, J.: Adam: A method for stochastic optimization, in: *International Conference on Learning Representations (ICLR)*,  
San Diego, CA, USA, 2015.
- 545 Kumar, L. and Sinha, P.: Mapping salt-marsh land-cover vegetation using high-spatial and hyperspectral satellite data to assist wetland  
inventory, *GIScience & Remote Sensing*, 51, 483–497, <https://doi.org/10.1080/15481603.2014.947838>, 2014.
- Li, H., Wang, C., Cui, Y., and Hodgson, M.: Mapping salt marsh along coastal South Carolina using U-Net, *ISPRS Journal of Photogrammetry  
and Remote Sensing*, 179, 121–132, <https://doi.org/10.1016/j.isprsjprs.2021.07.011>, 2021a.
- Li, H., Zhang, C., Zhang, S., Ding, X., and Atkinson, P. M.: Iterative Deep Learning (IDL) for agricultural landscape classification using  
550 fine spatial resolution remotely sensed imagery, *International Journal of Applied Earth Observation and Geoinformation*, 102, 102437,  
<https://doi.org/10.1016/j.jag.2021.102437>, 2021b.
- Li, X., Tian, J., Li, X., Yu, Y., Ou, Y., Zhu, L., Zhu, X., Zhou, B., and Gong, H.: Annual mapping of *Spartina alterniflora* with deep learning  
and spectral-phenological features from 2017 to 2021 in the mainland of China, *International Journal of Remote Sensing*, 45, 3172–3199,  
<https://doi.org/10.1080/01431161.2024.2343136>, 2024a.

- 555 Li, Y., Yuan, L., Song, Z., Yu, S., Zhang, X., Tian, B., and Liu, M.: Salt marsh carbon stock estimation using deep learning with Sentinel-1 SAR of the Yangtze River estuary, China, *International Journal of Applied Earth Observation and Geoinformation*, 133, 104 138, <https://doi.org/10.1016/j.jag.2024.104138>, 2024b.
- Li, Y., TingLiu, Yuan, L., Song, Z., Yang, S., Zhu, Z., and Liu, M.: CCAV-10m: An Annual Spatiotemporal China Coastal Wetland Vegetation Dataset Integrating Sentinel-1/2 Observations via Deep Learning, <https://doi.org/10.57760/sciencedb.31077>, 2025.
- 560 Luo, J., Wu, X., Gao, Y., Cai, Y., Yang, L., Xiong, Y., Yang, Q., Liu, J., Li, Y., Deng, Z., et al.: Spatiotemporal Variations and Seasonal Climatic Driving Factors of Stable Vegetation Phenology Across China over the Past Two Decades, *Remote Sensing*, 17, 3467, <https://doi.org/10.3390/rs17203467>, 2025.
- Luther, D. A. and Greenberg, R.: Mangroves: a global perspective on the evolution and conservation of their terrestrial vertebrates, *BioScience*, 59, 602–612, <https://doi.org/10.1525/bio.2009.59.7.11>, 2009.
- 565 Macreadie, P. I., Anton, A., Raven, J. A., Beaumont, N., Connolly, R. M., Friess, D. A., Kelleway, J. J., Kennedy, H., Kuwae, T., Lavery, P. S., et al.: The future of Blue Carbon science, *Nature communications*, 10, 3998, <https://doi.org/10.1038/s41467-019-11693-w>, 2019.
- Mahdianpari, M., Jafarzadeh, H., Granger, J. E., Mohammadimanesh, F., Brisco, B., Salehi, B., Homayouni, S., and Weng, Q.: A large-scale change monitoring of wetlands using time series Landsat imagery on Google Earth Engine: a case study in Newfoundland, *GIScience & Remote Sensing*, 57, 1102–1124, <https://doi.org/10.1080/15481603.2020.1846948>, 2020.
- 570 Mandal, D., Kumar, V., Ratha, D., Dey, S., Bhattacharya, A., Lopez-Sanchez, J. M., McNairn, H., and Rao, Y. S.: Dual polarimetric radar vegetation index for crop growth monitoring using sentinel-1 SAR data, *Remote Sensing of Environment*, 247, 111 954, <https://doi.org/10.1016/j.rse.2020.111954>, 2020.
- Mao, W., Wang, X., Liu, G., Pirasteh, S., Zhang, R., Lin, H., Xie, Y., Xiang, W., Ma, Z., and Ma, P.: Time series InSAR ionospheric delay estimation, correction, and ground deformation monitoring with reformulating range split-spectrum interferometry, *IEEE Transactions on Geoscience and Remote Sensing*, 61, 1–18, <https://doi.org/10.1109/TGRS.2023.3298919>, 2023.
- 575 Min, Y., Ke, Y., Zhuo, Z., Qi, W., Li, J., Li, P., and Zhao, N.: Monitoring *Spartina Alterniflora* removal dynamics across coastal China using time series Sentinel-1 imagery, *Remote Sensing of Environment*, 326, 114 813, <https://doi.org/10.1016/j.rse.2025.114813>, 2025.
- Mleczko, M. and Mróz, M.: Wetland mapping using sar data from the sentinel-1a and tandem-x missions: A comparative study in the biebza floodplain (Poland), *Remote Sensing*, 10, 78, <https://doi.org/10.3390/rs10010078>, 2018.
- 580 Morales-Barquero, L., Lyons, M. B., Phinn, S. R., and Roelfsema, C. M.: Trends in remote sensing accuracy assessment approaches in the context of natural resources, *Remote sensing*, 11, 2305, <https://doi.org/10.3390/rs11192305>, 2019.
- Moreno-Mateos, D., Power, M. E., Comín, F. A., and Yockteng, R.: Structural and functional loss in restored wetland ecosystems, *PLoS biology*, 10, e1001 247, <https://doi.org/10.1371/journal.pbio.1001247>, 2012.
- Murray, N. J., Worthington, T. A., Bunting, P., Duce, S., Hagger, V., Lovelock, C. E., Lucas, R., Saunders, M. I., Sheaves, M., Spalding, M.,  
585 et al.: High-resolution mapping of losses and gains of Earth’s tidal wetlands, *Science*, 376, 744–749, 2022.
- Nikaein, T., Iannini, L., Molijn, R. A., and Lopez-Dekker, P.: On the value of Sentinel-1 InSAR coherence time-series for vegetation classification, *Remote Sensing*, 13, 3300, <https://doi.org/10.3390/rs13163300>, 2021.
- O’Connell, J. L., Mishra, D. R., Cotten, D. L., Wang, L., and Alber, M.: The Tidal Marsh Inundation Index (TMII): An inundation filter to flag flooded pixels and improve MODIS tidal marsh vegetation time-series analysis, *Remote Sensing of Environment*, 201, 34–46,  
590 <https://doi.org/10.1016/j.rse.2017.08.008>, 2017.

- Potin, P., Rosich, B., Grimont, P., Miranda, N., Shurmer, I., O'Connell, A., Torres, R., and Krassenburg, M.: Sentinel-1 mission status, in: International Geoscience and Remote Sensing Symposium (IGARSS) (Vol. 2015–Novem), vol. 2015–Novem, pp. 2820–2823, IEEE, <https://doi.org/10.1109/IGARSS.2015.7326401>, 2015.
- Rajngewerc, M., Grimson, R., Bali, L., Minotti, P., and Kandus, P.: Cover classifications in wetlands using Sentinel-1 data (Band C): a case study in the Parana river delta, Argentina, *Revista de Teledetección*, pp. 29–46, <https://doi.org/10.4995/raet.2022.16915>, 2022.
- Schuerch, M., Spencer, T., Temmerman, S., Kirwan, M. L., Wolff, C., Lincke, D., McOwen, C. J., Pickering, M. D., Reef, R., Vafeidis, A. T., et al.: Future response of global coastal wetlands to sea-level rise, *Nature*, 561, 231–234, <https://doi.org/10.1038/s41586-018-0476-5>, 2018.
- Service, L. P. M.: Main Meteorological Disasters and Early Warning Signals in Liaoning Province, August 2023, Meteorological bulletin, Liaoning Provincial Meteorological Service, Shenyang, [http://ln.cma.gov.cn/xwzx/qxxw/202309/t20230905\\_5757479.html](http://ln.cma.gov.cn/xwzx/qxxw/202309/t20230905_5757479.html), released on 2023-09-05, 2023.
- Simioni, J. P. D., Guasselli, L. A., Nascimento, V. F., Ruiz, L. F. C., and Belloli, T. F.: Integration of multi-sensor analysis and decision tree for evaluation of dual and quad-Pol SAR in L-and C-bands applied for marsh delineation, *Environ. Dev. Sustain*, 22, 5603–5620, <https://doi.org/10.1007/s10668-019-00442-0>, 2020.
- Slagter, B., Tsendbazar, N.-E., Vollrath, A., and Reiche, J.: Mapping wetland characteristics using temporally dense Sentinel-1 and Sentinel-2 data: A case study in the St. Lucia wetlands, South Africa, *International Journal of Applied Earth Observation and Geoinformation*, 86, 102 009, <https://doi.org/10.1016/j.jag.2019.102009>, 2020.
- Song, Z. and Zhong, B.: A lightweight local-global attention network for single image super-resolution, in: Proceedings of the Asian conference on computer vision, pp. 4395–4410, [https://doi.org/10.1007/978-3-031-26351-4\\_37](https://doi.org/10.1007/978-3-031-26351-4_37), 2022.
- Sun, B., Zhang, D., and Lai, Z.: Coastal salt marsh vegetation classification using hybrid convolutional neural networks and spectral index time series images, *Ecological Indicators*, 178, 113 996, <https://doi.org/10.1016/j.ecolind.2025.113996>, 2025.
- Sun, C., Li, J., Liu, Y., Liu, Y., and Liu, R.: Plant species classification in salt marshes using phenological parameters derived from Sentinel-2 pixel-differential time-series, *Remote Sensing of Environment*, 256, 112 320, <https://doi.org/10.1016/j.rse.2021.112320>, 2021.
- Sun, C., Li, J., Liu, Y., Zhao, S., Zheng, J., and Zhang, S.: Tracking annual changes in the distribution and composition of saltmarsh vegetation on the Jiangsu coast of China using Landsat time series–based phenological parameters, *Remote Sensing of Environment*, 284, 113 370, <https://doi.org/10.1016/j.rse.2022.113370>, 2023.
- Sun, L.: Survey Dataset of Wetland Plants in Coastal Areas of China (2013–2017), <https://doi.org/10.57760/sciencedb.IGA.00342>, 2023.
- Sun, Z., Sun, W., Tong, C., Zeng, C., Yu, X., and Mou, X.: China's coastal wetlands: conservation history, implementation efforts, existing issues and strategies for future improvement, *Environment International*, 79, 25–41, <https://doi.org/10.1016/j.envint.2015.02.017>, 2015.
- Takeuchi, W., Tamura, M., and Yasuoka, Y.: Estimation of methane emission from West Siberian wetland by scaling technique between NOAA AVHRR and SPOT HRV, *Remote Sensing of Environment*, 85, 21–29, [https://doi.org/10.1016/S0034-4257\(02\)00183-9](https://doi.org/10.1016/S0034-4257(02)00183-9), 2003.
- Tian, J., Wang, L., Yin, D., Li, X., Diao, C., Gong, H., Shi, C., Menenti, M., Ge, Y., Nie, S., et al.: Development of spectral-phenological features for deep learning to understand *Spartina alterniflora* invasion, *Remote Sensing of Environment*, 242, 111 745, <https://doi.org/10.1016/j.rse.2020.111745>, 2020.
- Van Beijma, S., Comber, A., and Lamb, A.: Random forest classification of salt marsh vegetation habitats using quad-polarimetric airborne SAR, elevation and optical RS data, *Remote Sensing of Environment*, 149, 118–129, <https://doi.org/10.1016/j.rse.2014.04.010>, 2014.

- Veloso, A., Mermoz, S., Bouvet, A., Le Toan, T., Planells, M., Dejoux, J.-F., and Ceschia, E.: Understanding the temporal behavior of crops using Sentinel-1 and Sentinel-2-like data for agricultural applications, *Remote Sens. Environ.*, 199, 415–426, <https://doi.org/10.1016/j.rse.2017.07.015>, 2017.
- 630 Vreugdenhil, M., Wagner, W., Bauer-Marschallinger, B., Pfeil, I., Teubner, I., Rüdiger, C., and Strauss, P.: Sensitivity of Sentinel-1 backscatter to vegetation dynamics: An Austrian case study, *Remote Sensing*, 10, 1396, <https://doi.org/10.3390/rs10091396>, 2018.
- Wang, X., Xiao, X., Xu, X., Zou, Z., Chen, B., Qin, Y., Zhang, X., Dong, J., Liu, D., Pan, L., et al.: Rebound in China's coastal wetlands following conservation and restoration, *Nature Sustainability*, 4, 1076–1083, <https://doi.org/10.1038/s41893-021-00793-5>, 2021.
- Wang, Y., Jin, S., and Dardanelli, G.: Vegetation classification and evaluation of yancheng coastal wetlands based on random forest algorithm  
635 from sentinel-2 images, *Remote Sensing*, 16, 1124, <https://doi.org/10.3390/rs16071124>, 2024.
- Webb, E. L., Friess, D. A., Krauss, K. W., Cahoon, D. R., Guntenspergen, G. R., and Phelps, J.: A global standard for monitoring coastal wetland vulnerability to accelerated sea-level rise, *Nature Climate Change*, 3, 458–465, <https://doi.org/10.1038/nclimate1756>, 2013.
- Wei, S., Zhang, H., Xu, Z., Lin, G., Lin, Y., Liang, X., Ling, J., Wee, A. K. S., Lin, H., Zhou, Y., et al.: Coastal urbanization may indirectly positively impact growth of mangrove forests, *Communications Earth & Environment*, 5, 608, [https://doi.org/10.1038/s43247-024-01776-](https://doi.org/10.1038/s43247-024-01776-y)  
640 [y](https://doi.org/10.1038/s43247-024-01776-y), 2024.
- Wu, Y., Dai, L., Wang, Y., Xie, L., Zhao, S., Liu, Y., Zhang, M., and Zhang, Z.: Coexistence mechanisms of *Tamarix chinensis* and *Suaeda salsa* in the Yellow River Delta, China, *Environmental Science and Pollution Research*, 27, 26 172–26 181, <https://doi.org/10.1007/s11356-020-08883-1>, 2020.
- Xu, R., Fan, Y., Fan, B., Feng, G., and Li, R.: Classification and Monitoring of Salt Marsh Vegetation in the Yellow River Delta Based on  
645 Multi-Source Remote Sensing Data Fusion, *Sensors*, 25, 529, <https://doi.org/10.3390/s25020529>, 2025.
- Yang, R.-M. and Guo, W.-W.: Using Sentinel-1 imagery for soil salinity prediction under the condition of coastal restoration, *IEEE Journal of Selected Topics in Applied Earth Observations and Remote Sensing*, 12, 1482–1488, <https://doi.org/10.1109/JSTARS.2019.2906064>, 2019.
- You, S., Loh, P., Li, Z., Qin, H., Pradit, S., Le, T. P. Q., Oeurng, C., Mohamed, C. A. R., Lee, C. W., Lu, X., et al.: Geochemical behavior of  
650 sedimentary phosphorus species in northernmost artificial mangroves in China, *Forests*, 13, 610, <https://doi.org/10.3390/f13040610>, 2022.
- Zeng, J., Sun, Y., Cao, P., and Wang, H.: A phenology-based vegetation index classification (PVC) algorithm for coastal salt marshes using Landsat 8 images, *International Journal of Applied Earth Observation and Geoinformation*, 110, 102 776, <https://doi.org/10.1016/j.jag.2022.102776>, 2022.
- Zhang, A., Sun, G., Ma, P., Jia, X., Ren, J., Huang, H., and Zhang, X.: Coastal wetland mapping with Sentinel-2 MSI im-  
655 agery based on gravitational optimized multilayer perceptron and morphological attribute profiles, *Remote Sensing*, 11, 952, <https://doi.org/10.3390/rs11080952>, 2019.
- Zhang, B., Wdowinski, S., Gann, D., Hong, S.-H., and Sah, J.: Spatiotemporal variations of wetland backscatter: The role of water depth and vegetation characteristics in Sentinel-1 dual-polarization SAR observations, *Remote Sensing of Environment*, 270, 112 864, <https://doi.org/10.1016/j.rse.2021.112864>, 2022a.
- 660 Zhang, C., Gong, Z., Qiu, H., Zhang, Y., and Zhou, D.: Mapping typical salt-marsh species in the Yellow River Delta wetland supported by temporal-spatial-spectral multidimensional features, *Science of the total environment*, 783, 147 061, <https://doi.org/10.1016/j.scitotenv.2021.147061>, 2021.
- Zhang, J., Chen, S., Wu, Z., and Fu, Y. H.: Review of vegetation phenology trends in China in a changing climate, *Progress in Physical Geography: Earth and Environment*, 46, 829–845, <https://doi.org/10.1177/03091333221114737>, 2022b.

- 665 Zhang, J., Zhang, Y., Cong, N., Tian, L., Zhao, G., Zheng, Z., Gao, J., Zhu, Y., and Zhang, Y.: Coarse spatial resolution remote sensing data with AVHRR and MODIS miss the greening area compared with the Landsat data in Chinese drylands, *Frontiers in Plant Science*, 14, 1129 665, <https://doi.org/10.3389/fpls.2023.1129665>, 2023a.
- Zhang, X., Liu, L., Zhao, T., Chen, X., Lin, S., Wang, J., Mi, J., and Liu, W.: GWL\_FCS30: global 30 m wetland map with fine classification system using multi-sourced and time-series remote sensing imagery in 2020, *Earth System Science Data Discussions*, 2022, 1–31, 670 <https://doi.org/10.5194/essd-15-265-2023>, 2022c.
- Zhang, X., Zhao, T., Xu, H., Liu, W., Wang, J., Chen, X., and Liu, L.: GLC\_FCS30D: The first global 30-m land-cover dynamic monitoring product with a fine classification system from 1985 to 2022 using dense time-series Landsat imagery and continuous change-detection method, *Earth System Science Data Discussions*, 2023, 1–32, <https://doi.org/10.5194/essd-16-1353-2024>, 2023b.
- Zhao, C., Jia, M., Wang, Z., Mao, D., and Wang, Y.: Toward a better understanding of coastal salt marsh mapping: A case from China using 675 dual-temporal images, *Remote Sensing of Environment*, 295, 113 664, <https://doi.org/10.1016/j.rse.2023.113664>, 2023.
- Zhao, X., Nishina, K., Izumisawa, H., Masutomi, Y., Osako, S., and Yamamoto, S.: Monsoon Asia Rice Calendar (MARC): a gridded rice calendar in monsoon Asia based on Sentinel-1 and Sentinel-2 images, *Earth System Science Data*, 16, 3893–3911, <https://doi.org/10.5194/essd-16-3893-2024>, 2024.
- Zheng, J., Sun, C., Zhao, S., Hu, M., Zhang, S., and Li, J.: Classification of salt marsh vegetation in the Yangtze River Delta of China using 680 the pixel-level time-series and XGBoost algorithm, *Journal of Remote Sensing*, 3, 0036, <https://doi.org/10.1080/20964471.2025.2554043>, 2023.
- Zhou, D., Ni, Y., Yu, X., Lin, K., Du, N., Liu, L., Guo, X., and Guo, W.: Trait-based adaptability of *Phragmites australis* to the effects of soil water and salinity in the Yellow River Delta, *Ecology and Evolution*, 11, 11 352–11 361, 2021.